Altered inhibition and excitation in neocortical circuits in congenital microcephaly

Sami Zaqout, Kathrin Blaesius, Yuan-Ju Wu, Stefanie Ott, Nadine Kraemer, Lena-Luise Becker, Marta Rosário, Christian Rosenmund, Ulf Strauss, Angela M. Kaindl

Altered inhibition and excitation in neocortical circuits in congenital microcephaly

Sami Zaqout,[1-4][§] Kathrin Blaesius,[1-4][§] Yuan-Ju Wu,[5] Stefanie Ott,[1] Nadine Kraemer,[1-3] Lena-Luise Becker,[1-3] Marta Rosário,[1] Christian Rosenmund,[4,5,6] Ulf Strauss,[1][§] Angela M. Kaindl,[1-4][§][#]

[1]Charité – Universitätsmedizin Berlin, Institute of Cell- and Neurobiology, Charitéplatz 1, 10117 Berlin, Germany

[2]Charité – Universitätsmedizin Berlin, Center for Chronically Sick Children (Sozialpädiatrisches Zentrum, SPZ), Augustenburger Platz 1, 13353 Berlin, Germany

[3]Charité – Universitätsmedizin Berlin, Department of Pediatric Neurology, Augustenburger Platz 1, 13353 Berlin, Germany

[4]Berlin Institute of Health (BIH), Anna-Louisa-Karsch Strasse 2, 10178 Berlin, Germany

[5]Charité – Universitätsmedizin Berlin, NeuroCure, Charitéplatz 1, 10117 Berlin, Germany

[6]Charité – Universitätsmedizin Berlin, Institute of Neurophysiology, Charitéplatz 1, 10117 Berlin, Germany

[§]These authors contributed equally to this work.

[#]Corresponding author: Dr. Angela M. Kaindl, Institute for Cell Biology and Neurobiology, Charité - Universitätsmedizin Berlin, Charitéplatz 1, 10117 Berlin. Tel/Fax: +49 (0)30 450 566112/920. Email: angela.kaindl@charite.de.

Running title

Cdk5rap2 and neocortical E/I balance

1 **Abstract**

2 Congenital microcephaly is highly associated with intellectual disability. Features of autosomal

3 recessive primary microcephaly subtype 3 (MCPH3) also include hyperactivity and seizures.

4 The disease is caused by biallelic mutations in the Cyclin-dependent kinase 5 regulatory

5 subunit-associated protein 2 gene *CDK5RAP2*. In the mouse, *Cdk5rap2* mutations similar to

6 the human condition result in reduced brain size and a strikingly thin neocortex already at early

7 stages of neurogenesis that persists through adulthood. The microcephaly phenotype in MCPH

8 arises from a neural stem cell proliferation defect. Here, we report a novel role for Cdk5rap2 in

9 the regulation of dendritic development and synaptogenesis of neocortical layer 2/3 pyramidal

10 neurons. Cdk5rap2-deficient murine neurons show poorly branched dendritic arbors and an

11 increased density of immature thin spines and glutamatergic synapses *in vivo*. Moreover, the

12 excitatory drive is enhanced in *ex vivo* brain slice preparations of *Cdk5rap2* mutant mice.

13 Concurrently, we show that pyramidal neurons receive fewer inhibitory inputs. Together, these

14 findings point towards a shift in the excitation - inhibition balance towards excitation in

15 *Cdk5rap2* mutant mice. Thus, MCPH3 is associated not only with a neural progenitor

16 proliferation defect but also with altered function of postmitotic neurons and hence with altered

17 connectivity.

18

19 **Key words**

1. Introduction

Autosomal recessive primary microcephaly (MicroCephaly Primary Hereditary; MCPH) is a rare neurodevelopmental disorder characterized by intellectual disability and microcephaly at birth due to severe reduction in brain volume that affects especially the neocortex (Kaindl et al., 2010; Kraemer et al., 2011). So far, twenty genes have been linked to MCPH and are referred to as MCPH1-20 (DiStasio et al., 2017; Kadir et al., 2016; Moawia et al., 2017; reviewed in Zaqout et al., 2017b). Some MCPH patients have epilepsy and/or a hyperactivity disorder (Passemard et al., 2009). Biallelic mutations in the gene encoding centrosomal Cyclin-dependent kinase 5 regulatory subunit-associated protein 2 (CDK5RAP2) lead to MCPH3 (MIM*604804) (Bond et al., 2005; Hassan et al., 2007; Issa et al., 2013b).

MCPH is seen as model disorder for microcephaly. Thus, unraveling pathomechanisms of this disease can convey insight into basic mechanisms of physiologic brain development, particularly of brain growth and cortex formation. One current model for the microcephaly phenotype in MCPH invokes a premature shift from symmetric to asymmetric cell divisions and thus premature neurogenesis with a subsequent depletion of the progenitor pool (Buchman et al., 2010; Fish et al., 2006; Lizarraga et al., 2010). In addition, increased apoptosis of neural progenitors and postmitotic cells has been reported in MCPH3 mice (Kraemer et al., 2015; Lizarraga et al., 2010). Premature neurogenesis due to CDK5RAP2 dysfunction may be secondary to disturbances in cleavage plane orientation of apical neural progenitors (Lizarraga et al., 2010), altered centriole engagement and cohesion (Barrera et al., 2010), microtubule organizing dysfunction of the centrosome through interaction with the gamma tubulin ring complex (Fong et al., 2008), improper spindle formation and chromosome segregation (Bond et al., 2005). Most studies regarding the pathophysiology of MCPH have focused on division and survival of neural progenitors. The effect of MCPH proteins on neuronal differentiation and function within the neural circuit, however, has been largely neglected. Since a smaller brain does not necessarily imply intellectual disability but MCPH patients often display such condition together with hyperactivity, and in some cases epilepsy, we reasoned that MCPH proteins may have additional roles in postmitotic neurons, during synaptogenesis and synaptic transmission. Also, neurodevelopmental disorders associated with intellectual disability and neuropsychiatric conditions are often associated with defects in dendritic arborization and spine formation. We

52 have therefore addressed whether loss of Cdk5rap2 as seen in MCPH3 affects the function of

53 differentiated neurons in the neocortex by performing morphological and electrophysiological

54 studies on the established MCPH3 mouse model, *Cdk5rap2* mutant or *Hertwig's anemia* mice

55 (*an/an*). Our results demonstrate that Cdk5rap2 is essential for the maturation of the dendritic

56 arbor and its synaptic connectivity and affects dendritic structure and synaptic connectivity in

57 the mature brain.

58

59 **2. Results**

60 *2.1. Preserved neocortical layer organization but thin upper layers*

61 To address the role of Cdk5rap2 in mature neurons, we used the established *Cdk5rap2* mouse

62 model (*Hertwig's anemia* mice (*an/an*)) (Lizarraga et al., 2010). *Cdk5rap2* mutant mice (*an/an*)

63 display reduced overall brain size. Neocortical area was reduced to 46% and parietal cortical

64 thickness to 67% (Fig 1) at birth, in line with the findings reported by (Lizarraga et al., 2010).

65 These structural changes persisted into adulthood (reduction in neocortical area to 50% and

66 parietal cortical thickness to 68%; Fig 1) and were associated with a strong reduction in the

67 total number of cells in the neocortex of P0 and adult *an/an* mice (Fig 2A and B).

68   Cortical layer organization was grossly undisturbed, as revealed by immunostaining

69 with the layer 2-4 marker Cux1 and the layer 5-6 marker Ctip2 (Fig 2A). While both Cux1^{+} upper

70 layers and Ctip2^{+} deep layers were thinner (Fig 2C), only the relative thickness of upper layers

71 with respect to the total cortical thickness was reduced in P0 and adult *an/an* mice (Fig 2C and

72 S1 Table). The relative thickness of deep layers with respect to total cortical thickness remained

73 unchanged (Fig 2C). Cell counts per view-field were reduced for Cux1^{+} and Ctip2^{+} neocortical

74 neurons (Fig 2D and Table S1). However, the relative number of both Cux1^{+} and Ctip2^{+}

75 neocortical neurons (Fig 2D) with respect to total DAPI[+] nuclei was not changed, suggesting

76 that neuronal cell fate is unaltered. Together, these findings indicate that despite the large

77 reduction in cell numbers and cortical area, cortical architecture remains relatively undisturbed.

78

79 *2.2. Reduced dendritic complexity of layer 2/3 pyramidal neurons*

80 We next analyzed the dendritic tree of layer 2/3 neocortical neurons of adult *an/an* and

81 littermate +/+ mice in Golgi stained brain sections. We quantified the dendritic complexity of

82 individual neurons using Sholl analysis (SHOLL, 1953). Mutant *Cdk5rap2* in *an/an* mice is

83 associated with a downwards shift of the Sholl curve for both apical and basal dendrites of layer

84 2/3 pyramidal neurons, indicating a marked reduction in the complexity of these dendrites (Fig

85 3A, B and Fig. S2). In line, although the number of primary dendrites were similar (+/+ = 5.3 ±

86 0.2 *vs. an/an* = 4.9 ± 0.2 dendrites, p = 0.2, TT), numbers of secondary and tertiary dendrites

87 were reduced in *an/an* (secondary: +/+ = 10.4 ± 0.3 *vs. an/an* = 8.8 ± 0.3 dendrites, p < 0.002,

88 TT; tertiary: +/+ = 18.4 ± 1.3 vs. *an/an* = 10.5 ± 0.8 dendrites, p < 0.0001, TT; n = 44 +/+ and

89 39 *an/an* neurons from 6 +/+ and 4 *an/an* animals; Fig 3B).

90   As neuronal surface area and input resistance are inversely proportional, the reduction

91 in dendritic complexity could alter the intrinsic properties of *an/an* layer 2/3 neocortical neurons.

92 We therefore performed whole cell patch clamp recordings on these neurons. Indeed, when

93 compared to control neurons, *an/an* neurons showed an increased input resistance ($R_{in+/+}$ =

94 81.5 ± 8.6 MΩ, n = 15 *vs.* $R_{in an/an}$ = 153.5 ± 15.1 MΩ, n = 17, p < 0.001, MWU, Fig 3C) while

95 resting membrane potential remained similar ($V_{M+/+}$ = -79.1 ± 2.4 mV, n = 14 *vs.* $V_{M an/an}$ = -74.9

96 ± 2.5 mV, n = 10, p = 0.1, MWU). Accordingly, neuronal membrane capacitance was smaller

97 in *an/an* ($C_{+/+}$ = 125.7 ± 11.3 pF *vs.* $C_{an/an}$ = 94.9 ± 6.8 pF, p < 0.03, MWU). As a consequence,

98 the rheobase, i.e. the minimal current amplitude for action potential induction, decreased ($I_{rheo+/+}$

99 = 295.4 ± 23.6 pA, n = 13 *vs.* $I_{rheo an/an}$ 186.9 ± 44.3 pA, n = 13, p = 0.04 TT, Fig 3E and F) and

100 neuronal gain, given by the slope of the F/I relationship, increased ($F/I_{slope+/+}$ = 115.5 ± 14.9

101 AP/nA, n = 14 *vs.* $F/I_{slope an/an}$ = 159.6 ± 18.9 AP/nA, n = 13, p = 0.08, TT, Fig 3E and G). Thus,

102 our data imply that the reduced dendritic arborization of *an/an* neurons is associated with

103 intrinsic pro-excitatory neuronal properties. While reduced dendritic arborization may impact on

104 incoming dendritic signals by reducing the catchment area but increasing the electrotonic

105 compactness (Spruston et al., 1993), the latter properties putatively privilege small and remote

106 inputs.

107

108 ***2.3. Increased spine density, excitatory synapse number, and spontaneous***

109 ***glutamatergic transmission***

110 Our morphological findings and the fact that MCPH patients can suffer from hyperactive

111 behavior and seizures prompted us to study the dendritic spine and synapse properties of layer

112   2/3 neurons in adult *an/an* mice. We first analyzed dendritic spines in Golgi-stained pyramidal

113   neurons and found an increase in the density of spines along apical and basal dendrites (+/+

114   = 0.58 ± 0.04 µm^{-1} vs. *an/an* = 0.76 ± 0.03 µm^{-1}, p = 0.0007, TT, Fig 3H and I). We next

115   assessed whether spine morphology was altered in the mutants. We detected a significant

116   increase in the number of thin-shaped "immature" spines in *an/an* mice compared to +/+

117   littermates (+/+ = 16.2 ± 2.5 % *vs. an/an* = 28.5 ± 3.2 %, p < 0.005, TT, Fig 3H and I). Thin

118   spines, containing long necks and small spine heads, are thought to represent immature spines

119   (Dailey and Smith, 1996). To address whether the increase in spine density and altered spine

120   morphology results in a change in excitatory transmission, we recorded spontaneous excitatory

121   postsynaptic currents (sEPSCs) of layer 2/3 pyramidal neurons in *ex-vivo* adult brain slices (Fig

122   3J). sEPSCs mainly correspond to spontaneous presynaptic glutamate vesicle release

123   (Schuster et al., 2015), since spontaneous action potentials in layer 2/3 neurons in slices are

124   unlikely events. In accordance with the elevated spine density we found an increase in the total

125   excitatory charge transfer ($Q_{T+/+}$ = 1010.4 ± 135.3 fC, n = 15 *vs.* $Q_{Tan/an}$ = 1969.2 ± 460.2 fC, n

126   = 14, p < 0.05, MWU, Fig 3K) mainly due to an augmented sEPSCs frequency ($f_{+/+}$ = 18.1 ± 0.8

127   events/s, n = 15 *vs.* $f_{an/an}$ = 29.4 ± 1.6 events/s, n = 14, p < 0.0001, TT, Fig 3L), since sEPSC

128   kinetics were similar (decay: $\tau_{+/+}$ = 7.8 ± 0.6 ms, n = 15 *vs.* $\tau_{an/an}$ = 8.1 ± 0.8 ms, n = 14, p = 0.6,

129   MWU). The increase in frequency might be in part due to the reduced neuronal size in *an/an*

130   mice, making them electrically more compact and less leaky (Spruston et al., 1993).

131   Most of the additional spines in the mutant displayed "immature" thin spine morphology. Since

132   spine head width has been correlated to the level of AMPA receptors, this could suggest a

133   reduced number of AMPARs per spine (Matsuzaki et al., 2001). In our study mean EPSC

134   amplitude and amplitude density, as indirect measures of AMPA receptor number in the

135   postsynaptic density (Nair et al., 2013) did not differ between groups ($I_{+/+}$ = 10.5 ± 0.6 pA, n =

136   15 *vs. $I_{an/an}$* = 8.8 ± 0.7 pA, n = 14, p = 0.09, TT, Fig 3M, inset; $I/C_{+/+}$ = 0.092 ± 0.009 pA/pF, n

137   = 15 *vs. $I/C_{an/an}$* = 0.097 ± 0.008 pA, n = 14, p = 0.65, MWU), excluding an overall postsynaptic

138   phenotype in *an/an* neurons.

139   Survival to adulthood is a very rare event for *an/an* mice. To test whether the changes

140   in cell morphology was directly caused by the loss of gene function or rather the result of

141   secondary compensatory effects, we investigated layer 2/3 neuronal activity in *an/an* mice at

142 an early stage of synaptogenesis using *ex-vivo* P6/7 brain slices. At this stage of development,

143 we did not observe significant changes in membrane resistance, neuronal excitability ($R_{in+/+}$ =

144 598.6 ± 50.7 MΩ, n = 29 *vs.* $R_{in\,an/an}$ = 657.9 ± 53.6 MΩ, n = 35, p = 0.45; $I_{rheo+/+}$ = 29.2 ± 3.7 pA

145 *vs.* $I_{rheo\,an/an}$ = 35.8 ± 5.6 pA, p = 1, MWU; $FI_{slope+/+}$ = 334.5 ± 21.5 AP/nA, n = 29 *vs.* $FI_{slope\,an/an}$

146 = 421.1 ± 44.8 AP/nA, n = 35, p = 0.2, MWU; $V_{M+/+}$ = 72.6 ± 1.1 mV n = 22 *vs.* $V_{M\,an/an}$ = 68.9 ±

147 1.7 mV, n = 27, p = 0.2 Fig 4A – D) or neuronal membrane capacitance ($C_{+/+}$ = 75.1 ± 5.4 pF

148 *vs.* $C_{an/an}$ = 74.5 ± 4.1 pF, p = 0.99, MWU). This indicates comparable electrotonic compactness

149 at this stage, enabling us to investigate electrophysiological differences independent of gross

150 morphological changes. Excitatory synaptic drive was already elevated in the mutant as evident

151 by the 48% increase in total excitatory charge transfer ($Q_{T+/+}$ = 93.3 ± 16.6 fC, n = 23 *vs.* $Q_{T\,an/an}$

152 = 138.6 ± 18.3 fC, n = 28, p < 0.08, MWU; Fig 4F) and 53% increase in sEPSC frequency ($f_{+/+}$

153 = 2.18 ± 0.22 events/s, n = 29 *vs.* $f_{an/an}$ = 3.33 ± 0.27 events/s, n = 38, p = 0.008, MWU; Fig 4E

154 and G). This increase in frequency was not accompanied by a change in amplitude ($I_{+/+}$ = 6.24

155 ± 0.39 pA, n = 29 *vs.* $I_{an/an}$ = 5.84 ± 0.31 pA, n = 38, p = 0.3, MWU; Fig 4H), amplitude density

156 ($I/C_{+/+}$ = 0.087 ± 0.005 pA/pF, n = 29 *vs.* $I/C_{an/an}$ = 0.084 ± 0.005 pA, n = 38, p = 0.89, MWU) or

157 kinetics (decay: $\tau_{+/+}$ = 7.8 ± 0.5 ms, n = 29 *vs.* $\tau_{an/an}$ = 8.1 ± 0.6 ms, n = 38, p = 0.7, TT).

158 Changes in sEPSC frequency in P6-7 *an/an* mice are unlikely due to the detection of

159 more events from distal dendrites because electrical compactness was similar in both

160 genotypes. The increase could be mediated by changes in spontaneous presynaptic firing (but

161 see TTX-experiments under 2.5) or may be linked to presynaptic vesicle release probability

162 (del CASTILLO and KATZ, 1954). We therefore evoked paired pulse responses in layer 2/3

163 neocortical neurons but found no alteration in the paired pulse ratio of *an/an* cells (Fig 4I and

164 J), suggesting that presynaptic release probability is unaffected. Finally, immunohistochemical

165 staining for pre- (VGlut1) and postsynaptic (PSD95) markers revealed a 66% increase in

166 VGlut1/PSD95-positive synapses already at P6/7 in *an/an* layer 2/3 neurons (Fig 4K and L).

167 Taken together, these results point towards an increase in excitatory drive of layer 2/3

168 pyramidal neurons in *an/an* mice regardless of their age or severity of alteration (as indicated

169 by early death *vs.* survival).

170

171

172 ***2.4 Minor influence of Cdk5rap2 on dendritic complexity or excitatory transmission in***

173 ***cultured neocortical pyramidal neurons***

174 Altered Cdk5rap2 function may contribute, in a cell intrinsic fashion, to reduced dendritic

175 complexity and elevated excitatory drive of *an/an* mice layer 2/3 neurons. Cdk5rap2 has been

176 shown to interact with chromatin associated Cdc20-anaphase promoting complex (Cdc20-

177 APC) protein (Kraemer et al., 2011; X. Zhang et al., 2009) that can influence dendritic

178 development (Kim et al., 2009). Therefore, we investigated the effect of Cdk5rap2 loss of

179 function *in vitro*. We first used autaptic (i.e. singly cultured neurons) primary neuronal cultures

180 from newborn +/+ and *an/an* cortices that allow for detailed quantification of synaptic properties.

181 Neurons derived from *an/an* cultures had a reduced soma size ($A_{+/+}$ = 148.6 ± 7.7 μm^2, n = 28

182 vs. $A_{an/an}$ = 126.3 ± 5.6 μm^2, n = 38, p = 0.02, TT). We found no significant change in the total

183 length of dendrites ($L_{d+/+}$ = 962.9 ± 92.8 μm, n = 28 *vs.* $Ld_{an/an}$ = 878.8 ± 74.9 μm, n = 36, p =

184 0.7, MWU). The axonal length was reduced by nearly 30% when compared to those from +/+

185 cultures ($L_{a an/an}$ = 986.9 ± 159.8 μm, n = 23 *vs.* $L_{a+/+}$ = 1314.1 ± 172.1 μm, n = 17, p = 0.07,

186 MWU, Fig 5A and C). However, numbers of primary dendrites (+/+: 5.4 ± 0.6, n = 20; *an/an*:

187 5.7 ± 0.4, n = 31, p = 0.46, MWU) and dendritic tips (+/+: 20.9 ± 2.1, n = 20 *an/an*: 22.0 ± 1.6,

188 n = 31, p = 0.7, TT) did not differ between the groups, resulting in a comparable branching

189 index (+/+: 4.2 ± 0.4, n = 20, *an/an*: 5.7 ± 0.25, n = 31, p = 0.57, TT, Fig 5A and B).

190 We next analyzed the synaptic transmission of glutamatergic autaptic neurons but

191 found no significant difference in evoked responses (EPSCs; $I_{+/+}$ = 5.54 ± 0.67 nA, n = 65 *vs.*

192 $I_{an/an}$ = 5.15 ± 0.67 nA, n = 54, p = 0.64, MWU, Fig 5D) nor in mEPSC rates or amplitudes

193 between +/+ and *an/an* mouse neurons ($f_{+/+}$ = 2.3 ± 0.4 events/s, n = 52 *vs.* $f_{an/an}$ = 2.7 ± 0.4

194 events/s, n = 45, p = 0.3, MWU; $I_{+/+}$ = 24.5 ± 1.7 pA, n = 52 *vs.* $I_{an/an}$ = 23.6 ± 1.3 pA, n = 45, p

195 = 0.9, MWU; Fig 5H to J). Utilizing responses induced by hypertonic solution, we next

196 determined the size of the readily releasable pool (RRP = the amount of primed synaptic

197 vesicles; (Rosenmund and Stevens, 1996)) in *an/an* compared to +/+ neurons and found,

198 consistent with the unchanged evoked response, no alteration between wildtype and mutant

199 neurons ($RRP_{+/+}$ = 307.2 ± 51.4 pC, n = 51 *vs.* $RRP_{an/an}$ = 416.5 ± 71.5 pC, n = 44, p = 0.3,

200 MWU; Fig 5E and F). The vesicular release probability (Pvr), as calculated by comparing

201 evoked response and RRP size, was also comparable between +/+ and *an/an* neurons ($Pvr_{+/+}$

202   = 11.7 ± 0.9 %, n = 51 *vs.* $Pvr_{an/an}$ = 10.6 ± 0.9 %, n = 44, p = 0.9, TT, Fig 5G).

203   We further examined synapse formation on cortical neurons in dissociated cultures

204   and found no differences. In detail, the density of glutamatergic presynaptic punctae was

205   comparable (Fig 5K; VGlut1; +/+ = 3140 ± 249 puncta/0.15 mm^2, n = 38 *vs. an/an* = 3487 ±

206   300 puncta/0.15mm^2, n = 37, p = 0.4, MWU; from 3 independent cultures). Taken together, our

207   results from the cultured neurons imply that changes induced by *Cdk5rap2* mutation are not

208   entirely cell intrinsic and require *in-vivo* like neuron-neuron interactions. Note that these results

209   do not exclude an astrocytic malfunction in *an/an*, because both, autaptic and continental

210   neuronal cultures were grown on non-mutated feeder astrocytes.

211

2.5. Decreased inhibitory tone in ex-vivo slices of Cdk5rap2 mutants

213   Given the observed increased excitatory drive at the soma of pyramidal *Cdk5rap2* mutant

214   neurons *ex-vivo* but not in singly cultured neurons and the known control of pyramidal neurons

215   by inhibitory neurons, we again drew upon brain slice experiments to analyze the importance

216   of neuronal interaction for the Cdk5rap2 phenotype. We first examined the inhibitory tone in

217   *ex-vivo* brain slices by quantifying miniature inhibitory postsynaptic currents (mIPSC) (Fig 6A).

218   At P6-7, we found that the *Cdk5rap2* mutation is associated with decreased inhibitory charge

219   transfer ($Q_{T+/+}$ = 126.3 ± 13.5 fC, n = 30 *vs.* $Q_{Tan/an}$ = 102.4 ± 12.9 fC, n = 32, p < 0.03, MWU,

220   Fig 6B). A comparison of frequency and amplitude of mIPSC events showed that the decreased

221   tone was most likely due to the decreased frequency of events ($f_{+/+}$ = 1.40 ± 0.05 events/s *vs.*

222     $f_{an/an}$ = 1.04 ± 0.05 events/s, p < 0.0001, MWU) because mIPSC amplitude ($I_{+/+}$ = 11.36 ± 0.95

223   pA, n = 30 *vs.* $I_{an/an}$ = 12.28 ± 0.94 pA, n = 32, p = 0.2, MWU, Fig 6C and D), amplitude density

224   ($I/C_{+/+}$ = 0.129 ± 0.009 pA/pF *vs.* $I/C_{an/an}$ = 0.131 ± 0.009 pA, p = 0.86, TT), mIPSC kinetics

225   (decay: $\tau_{+/+}$ = 8.34 ± 0.21 ms, n = 30 *vs.* $\tau_{an/an}$ = 8.62 ± 0.46 ms, n = 32, p = 0.8, MWU) and

226   neuronal membrane capacitance ($C_{+/+}$ = 90.2 ± 13.1 pF *vs.* $C_{an/an}$ = 89.0 ± 8.3 pF, p = 0.7,

227   MWU) were similar in both genotypes. This indicates that less inhibitory synapses are formed

228   on pyramidal neurons already in emerging neural networks, which suggests that the density

229   and/or axonal tree formation of inhibitory neurons is impaired.

230   The ability of synapse formation itself was not disturbed in cultured GABAergic autaptic

231   neurons (Fig 6E) of *an/an* mice as synaptic transmission was comparable in the two groups. In

232   particular, evoked responses were similar in both genotypes (IPSCs; $I_{+/+}$ = 4.81 ± 1.41 nA, n =

233   8 *vs.* $I_{an/an}$ = 4.13 ± 2.57 nA, n = 15, p = 0.62, TT, Fig 6F and G). Consistent with the unchanged

234   evoked response, RRP size (RRP$_{+/+}$ = 2592.8 ± 650.3 pC, n = 8 *vs.* RRP$_{an/an}$ = 2179.7 ± 274.1

235   pC, n = 14, p = 0.6, 77; Fig 6H and I) and Pvr (Pvr$_{+/+}$ = 12.1 ± 3.0 %, n = 8 *vs.* Pvr$_{an/an}$ = 16.5 ±

236   2.6 %, n = 44, p = 0.9, TT, Fig 6J) were also comparable between +/+ and *an/an* mice. Finally,

237   mIPSC rates or amplitudes of +/+ and *an/an* mouse neurons (f$_{+/+}$ = 0.7 ± 0.2 events/s, n = 4 *vs.*

238   f$_{an/an}$ = 0.9 ± 0.4 events/s, n = 9, p = 0.5, MWU; $I_{+/+}$ = 32.7 ± 9.2 pA, n = 4 *vs.* $I_{an/an}$ = 27.9 ± 4.5

239   pA, n = 9, p = 0.8, MWU; Fig 6K - M) and the number of inhibitory synapses (VGat; +/+ = 2513.1

240   ± 197.2 puncta/0.15 mm^2, n = 38 *vs. an/an* = 3007.5 ± 257.9 puncta/0.15 mm^2, n = 37, p = 0.2,

241   MWU, Fig 5J) were similar.

242   In search for a morphological correlate of decreased inhibition in *Cdk5rap2* mutant

243   mice, we stained the cortex for GABA, a marker for interneurons (Uematsu et al., 2008) that is

244   also expressed in astrocytes (Yoon and Lee, 2014). However, astrocytes do not substantially

245   contribute to the GABA$^+$ cells at P6-7 (Fig S4). The total number of GABA$^+$ cells in P6-7 *an/an*

246   mice was smaller (GABA$^+_{+/+}$ = 71.0 ± 5.2 neurons per view-field, n = 6 animals *vs.* GABA$^+_{an/an}$

247   = 50.5 ± 7.1 neurons per view-field, n = 3 animals, p = 0.048, MWU; Fig 7A and B). This

248   reduction matches the general diminution of the neocortex since the relative proportion of these

249   neurons (compared to total NeuN$^+$ cells) was similar (GABA$^+$/NeuN$^+_{+/+}$ = 4.9 ± 0.5% n = 6

250   animals *vs.* GABA$^+$/NeuN$^+_{an/an}$ = 6.2 ± 0.6% n = 3 animals, p = 0.1, MWU; Fig 7A and B). In

251   contrast, we found a decrease in both the total number of GABA$^+$ interneurons in adult *an/an*

252   mice (GABA$^+_{+/+}$ = 37.3 ± 5.2 neurons per view-field, n = 6 animals *vs.* GABA$^+_{an/an}$ = 7.8 ± 1.5

253   neurons per view-field, n = 4 animals, p = 0.0095, MWU; Fig S3A and B) and in the relative

254   proportion of these neurons (GABA$^+$/NeuN$^+_{+/+}$ = 2.7 ± 0.4%, n = 6 animals *vs.*

255   GABA$^+$/NeuN$^+_{an/an}$ = 1.2 ± 0.2%, n = 4 animals, p = 0.0095, MWU; Fig S3A and B). In line with

256   the reduced mIPSC frequencies, layer 2/3 from P6-7 *an/an* mice showed a trend towards

257   decreased numbers of VGat$^+$ presynaptic inhibitory terminals in comparison to +/+ littermates

258   (+/+ = 110.3 ± 18.0 *vs. an/an* = 73.1 ± 8.2, p = 0.09, TT; Fig 7C and D). By co-staining the

259   same slices with VGlut1 and calculating the ratio of VGlut1 and VGat positive punctae we found

260   a markedly increased morphological excitation to inhibition (E/I) ratio of layer 2/3 neurons in

261   *an/an* mice (+/+ = 1.3 ± 0.2 *vs. an/an* = 2.4 ± 0.2, p = 0.003, TT; Fig 7D) as a result of a

262 decrease in inhibitory relative to excitatory (see also Fig 4K and L) synapses. This is roughly

263 in line with the functional E/I ratios calculated by dividing excitatory and inhibitory charge

264 transfers (+/+ = 1.14 ± 0.3 *vs.* an/an = 1.6 ± 0.2, p = 0.056, MWU). The reduced inhibition (less

265 mIPSCs and VGat positive terminals) is likely due to the decreased number of GABAergic

266 synapses in the cortex, since neither inhibitory quantal amplitude nor IPSC decay kinetic was

267 altered.

268   We reasoned that the reduced inhibitory influence observed in *an/an* neurons *ex-vivo*

269 contributes to an elevated frequency of glutamatergic signals at the soma. If our hypothesis

270 holds true, blocking GABAergic transmission should level out the differences in the number of

271 excitatory events between the groups (i.e. particularly increase the frequency of glutamatergic

272 signals in wild-types, similar to finding in *Cdk5rap2* mutants). We therefore applied the GABA$_A$

273 receptor blocker bicuculline (20 µM) to block inhibition and the sodium channel blocker

274 tetrodotoxin (1 µM) preventing increased pyramidal action potential firing induced by bicuculline

275 (Turrigiano et al., 1998) and putative spontaneous interneuronal action potentials. Indeed, this

276 treatment increased the frequency of excitatory events in +/+ (3.9 ± 0.4 to 5.5 ± 0.4 events/s,

277 n = 24, p = 0.02, ANOVA-RM-B in +/+) but not in *an/an* littermates at P6/7 (5.4 ± 0.4 to 5.8 ±

278 0.4 events/s, n = 22, p = 1, ANOVA-RM-B in *an/an* neurons) (Fig 7E - G). Note that in a subset

279 of experiments TTX alone did not change PSC frequencies in general (2.6 ± 0.3 *vs.* 2.8 ± 0.3

280 events/s, n = 17, p = 1, ANOVA-RM-B) or in on of the genotypes (1.8 ± 0.2 *vs.* 1.9 ± 0.3

281 events/s, n = 9 in +/+, and 3.6 ± 0.4 *vs.* 3.8 ± 0.4 events/s, n = 8 in *an/an*, p = 1, ANOVA-RM-

282 B, respectively). This also renders a contribution of increased presynaptic firing to the elevated

283 sEPSC frequencies in *an/an* mice (see 2.3) unlikely. We cannot, however, rule out that even in

284 the electrotonic compact neurons at P6-7 the increase in sEPSC frequency is caused by a

285 redistribution of the same number of excitatory inputs causing more EPSCs to be detected

286 somatically. Initial frequencies of sEPSC before blocking of GABA$_A$ receptors were again

287 increased in *an/an* compared to wild-type neurons (Fig 7F; p = 0.04, ANOVA-RM-B). Notably,

288 the excitatory charge transfers (Q$_{T+/+}$ = 151.0 ± 27.6 fC, n = 24 *vs.* Q$_{Tan/an}$ = 115.2 ± 16.3 fC, n

289 = 22, p = 0.3, ANOVA-RM-B) including mEPSC frequencies (p = 0.6), quantal mEPSC

290 amplitudes (*I*$_{+/+}$ = 6.7 ± 0.9 pA, n = 24 *vs.* *I*$_{an/an}$ = 5.4 ± 0.8 pA, n = 22, p = 0.5) and mEPSC

291 kinetics (decay: $\tau_{+/+}$ = 4.8 ± 0.3 ms, n = 24 *vs.* $\tau_{an/an}$ = 4.2 ± 0.2 ms, n = 22, p = 0.2, all ANOVA-

292 RM-B) did not differ between neurons from +/+ and *an/an* animals after blocking inhibition.

293 Neuronal membrane capacitance ($C_{+/+}$ = 70.8 ± 4.0 pF *vs.* $C_{an/an}$ = 84.8 ± 9.8 pF, p < 0.09,

294 MWU) and amplitude density ($I/C_{+/+}$ = 0.088 ± 0.010 pA/pF, n = 24 *vs.* $I/C_{an/an}$ = 0.065 ± 0.010

295 pA, n = 22, p = 0.51, ANOVA-RM-B) were comparable in +/+ and *an/an* neurons. Together

296 these results suggest that the elevated excitatory drive at the soma detected in *an/an* mice is

297 related to reduced inhibitory $GABA_A$ mediated transmission.

298

299 **3. Discussion**

300 Reduced brain size in patients with MCPH has been attributed to an abnormal proliferation of

301 neural progenitors. Here we show that Cdk5rap2 also regulates the differentiation of neocortical

302 neurons and the establishment of the neocortical circuit.

303 We demonstrate that the profound developmental reduction in brain size, cortical

304 thickness and neuron numbers in the *an/an* mouse model of MCPH3 (Lizarraga et al., 2010)

305 persists into adulthood (Fig 1). Brain size in itself does not necessarily imply dysfunctionality.

306 Therefore, we investigated whether the malfunction of microcephaly-associated protein

307 Cdk5rap2 results in additional cellular and functional defects that contribute to the neurologic

308 phenotype. Perhaps our most striking finding is that the *Cdk5rap2* mutation impacts the

309 establishment and function of neocortical circuits, whilst pyramidal cell fate specification and

310 cortical layering remain grossly unaltered (Fig 2). In particular, a*n/an* mice are distinguished by

311 an enhanced excitatory drive of neocortical pyramidal neurons during synaptogenesis and in

312 adulthood. We performed multiple experiments to further dissect the underlying mechanism: **1**)

313 On the *in vitro* level of individual isolated neurons neither morphological nor physiological

314 differences between neocortical neurons of *an/an* mice and their wild-type litters were present

315 (Fig 5 and 6). This finding suggests a dysfunction developing network (including astrocytes)

316 rather than mere cell autonomous mechanisms. **2**) In *ex-vivo* slices from adult *an/an* mice we

317 found simplified dendritic arbors with increased thin "immature" spines to be accompanied by

318 an increase in both intrinsic excitability and (extrinsic) excitatory drive on single layer 2/3

319 pyramidal neurons. **3**) To address the question whether the increase in excitatory drive is a

320 secondary effect, i.e., results from increased intrinsic excitability, we investigated layer 2/3

321 neurons at an early stage of synaptogenesis. The overall increased excitatory drive in the

322   mutants seems of primary synaptic origin, since the increased excitatory drive was not

323   accompanied by a change in intrinsic excitability (Fig 4). The increased excitatory drive was

324   accompanied by reduced inhibition (Fig 6). **4**) In line with the electrophysiological data, we

325   detected an increase overall number of excitatory synapses and a reduced number of inhibitory

326   synapses in the cortex (Fig 4 and 6). This imbalance in the number of excitatory to inhibitory

327   synapses on a morphologic level in the cortex, however, does not specifically pinpoint the

328   finding to pyramidal neurons. **5**) Addressing the role of inhibition in the pathomechanism of

329   MCPH, we found that blocking of GABAergic inhibition levels the excitatory drive of pyramidal

330   neurons of *an/an* and wild-type littermates (Fig 7), arguing that the increased excitatory drive

331   is related to a primary lack of inhibition. We cannot exclude a contribution of astrocytic

332   malfunction, although at P6-7 no obvious morphological differences were detected (Fig S4).

333   Altogether, we conclude that the increase in excitability is due to a shift in the balance of

334   excitation and inhibition and that the predominant effect of Cdk5Rap2 mutation on the network

335   level is loss of GABAergic tone onto pyramidal neurons.

336   Reduced inhibition might result either from a decrease in interneuron number or from

337   a failure of interneurons to integrate into functional networks for instances by an impaired ability

338   to form functional inhibitory synapses or both. We favor decreased inhibitory synapse formation

339   as primary cause at early stages (Fig 6) putatively resulting in reduced interneuron density at

340   later stages (Fig S3). Inhibitory inputs originate from interneurons that play an important

341   regulatory role in brain development (Cossart, 2011) and migrate tangentially from the

342   ganglionic eminence into the cortical plate to integrate into local circuits (Guo and Anton, 2014).

343   Concurrently, Cdk5rap2 is highly expressed in the neocortex during neurogenesis and

344   neuronal differentiation (Issa et al., 2013a), but present at lower levels during synaptogenesis

345   that completes around P21. Loss of Cdk5rap2 prematurely shifts symmetric to asymmetric cell

346   division leading to the earlier generation of postmitotic neurons (Buchman et al., 2010). This

347   might impair the proper integration of interneurons into neocortical circuits on a spatio-temporal

348   level and lead to increased interneuron death (Tuncdemir et al., 2016). Our results pointing to

349   an impaired inhibition fit to the actual view on the importance of interneurons during neocortical

350   development. Interneurons are critical for the integration and transmission of incoming synaptic

351   inputs that drive maturation (Kilb, 2012), since functional GABAergic connections regulate

352 network connectivity and excitation of pyramidal neurons (Isaacson and Scanziani, 2011). At

353 early stages of cortical development, i.e. when neurons assume their positions and begin to

354 mature, GABAergic inputs are required for the proper development of dendritic arbors and

355 excitatory synaptic inputs (Maric et al., 2001; Wang and Kriegstein, 2009; 2008). Aberrant

356 synaptic connections may lead to excessive dendritic pruning contributing to the observed

357 simplified dendritic arbor. Thus, our findings of reduced dendritic complexity and reduced

358 inhibition are in line with these previous reports.

359 Maturation of inhibitory synaptic contacts on the soma of somatosensory neurons, in

360 turn, depends on proper circuit function because it is impaired upon deficits in early activity or

361 sensory experience (Chattopadhyaya et al., 2004; Jiao et al., 2006; Xue et al., 2014). Notably,

362 in a previous study on adult neocortical layer 2/3 pyramidal neurons (Schuster et al., 2015) we

363 did not detect an increase in EPSC frequency after blocking inhibition. This supports the view

364 that during early synaptogenesis in (wild-type) mice GABA release results in more ambient

365 GABA and suggest that this developmental regulation is impaired in *an/an* mice. Since cortical

366 processing relies on the fine-tuned interplay between excitation and inhibition, healthy brains

367 exhibit a tight control of E/I ratio in all cortical areas even after perturbations (House et al.,

368 2011; Xue et al., 2014). This control is usually ensured by several regulators of E/I adjustment

369 (House et al., 2011; Lin et al., 2008; Rico and Marín, 2011; Xue et al., 2014). Our results in

370 *Cdk5rap2* mutants argue for an impaired E/I set point regulation as putatively caused by

371 improper expression or targeting of molecules that control synaptic specificity. In line, our

372 results of reduced number of inhibitory contacts while excitatory synapses and EPSC frequency

373 was increased in *an/an* are mimicked when PSD95 amount was increased experimentally

374 (Prange et al., 2004). Alternatively, inhibitory synaptogenesis might be regulated without E/I

375 balance compensation as shown for Npas4 (Lin et al., 2008).

376 Transient networks involve specific types of interneurons in deep and superficial layers

377 of the neocortex (Lim et al., 2018) and the 2 most prevalent early born interneuron populations

378 are SST[+] and PV[+], both generated in the MGE (Rudy et al., 2011). Since PV^{+} neurons largely

379 synapse on the soma of pyramidal neurons (Buhl et al., 1994) and are easy to recruit (Lazarus

380 and Huang, 2011) they might represent a major source of early mIPSCs (Soltesz et al., 1995).

381 PV^{+} neurons that do not fulfill their inhibitory role might contribute to cognitive deficits (Marín,

382 2012) due to perturbed perisomatic and axo-axonic inhibition. This might lead to impaired

383 oscillatory activity in the γ-frequency range (30 - 80 Hz, (Draguhn and Buzsáki, 2004)),

384 disturbed perisomatic feed-forward inhibition and therewith-reduced temporal precision of

385 signal transduction in pyramidal neurons (Pouille and Scanziani, 2001) and misguided activity

386 flow in local circuits (Xiang et al., 1998). However, synapses of PV+ neurons (on pyramidal

387 neurons and between PV+) appear only at the end of the first postnatal week (Pangratz-Fuehrer

388 and Hestrin, 2011) and might therefore contribute marginally to the observed effects. For the

389 GABAergic synapses that are present before that (Luhmann and Prince, 1991), SST+ provide

390 a putative source (Takesian and Hensch, 2013). The loss or disturbance of SST+ may cause

391 dysfunctional early transient networks and therewith impair the maturation of other interneurons

392 as PV+ basket cells (Tuncdemir et al., 2016). It is also conceivable that a SST+ neuronal loss /

393 dysfunction would lead to disturbed oscillatory activity in the β-frequency range (15 - 30 Hz,

394 (Draguhn and Buzsáki, 2004)).

395   Regardless of the cellular source, GABA reduction in the extracellular space might

396 influence neuronal development by impairing: a) neuronal migration in the embryonic cortex

397 (López Bendito et al., 2003), b) settlement of interneurons in the cortical plate (Bortone and

398 Polleux, 2009), c) formation of inhibitiory synapses (Oh et al., 2016) therewith setting the

399 balance between inhibitory and excitatory synapses in early postnatal stages as foundation of

400 later circuit development (Flores et al., 2015) and the neurogenesis of pyramidal neurons (Silva

401 et al., 2018).

402   Interpreting the functional role of increased excitatory synapses is not that

403 straightforward, given the lack of differences in excitatory drive after blocking inhibition (Fig 7).

404 If surplus excitatory synapses are on pyramidal neurons, they might be immature and silent. If

405 they are on interneurons, they might represent an insufficient homoeostatic mechanism to

406 increase inhibitory drive. In general, PV+ neurons receive strong excitatory input from pyramidal

407 neurons across and within layers and excitatory synapse number is modulated during

408 development (Chung et al., 2017). This modulation might influence the maturation of working

409 memory function since PV+ neurons are key intermediates in a disinhibitory circuit motif for

410 associative learning (Kepecs and Fishell, 2014).

411

412   Together, our results indicate that Cdk5rap2 influences E/I balance, dendrite

413   arborization and spine morphogenesis in layer 2/3 neocortical pyramidal neurons further

414   highlighting a connection between centrosomal biology and dendritic morphogenesis. These

415   data are in line with the clinical finding that some MCPH patients suffer from hyperactivity and

416   seizures. Since small dysregulations in E/I balance of cortical circuits, in particular due to

417   developmental disruptions of interneuron integration (Bartolini et al., 2013), can have dramatic

418   effects on entire cortical integration associated with the pathophysiology of neuropsychiatric

419   (eminently in developmental) diseases (Nelson and Valakh, 2015), further studies in humans

420   are warranted to analyze the significance of these findings for individuals with MCPH gene

421   mutations.

422

423   **4. Material and methods**

424   ***4.1. Mice***

425   All mouse experiments were carried out in accordance to state of Berlin rules (registration no.

426   T0309/09). *Cdk5rap2* mutant or *Hertwig's anemia* mice (*an/an*) carrying an inversion of exon 4

427   (leading to exon skipping; (Lizarraga et al., 2010)) were generated by crossing heterozygous

428   (*+/an*) mice (*C57BL/6* background; Jackson lab, stock no. 002306). Only 9.5% of the offspring

429   carried a homozygous mutant genotype (*an/an*) at birth due to *in utero* lethality (Zaqout et al.,

430   2017a). Most mutants die around postnatal day (P)7. Rare *an/an* mice surviving longer were

431   also used for morphological studies (n = 7) and electrophysiological recordings (n = 5; P30 -

432   80). Neurons were regarded as mature (Z.-W. Zhang, 2004) and none of the parameters was

433   correlated to age (table S2). The breeding was performed during the day, the day of birth was

434   designated as P0. Genotyping was confirmed by PCR primers for (+/+) F 5'-TC ACT GAG CTG

435   AAG AAG GAG AA-3', R 5'-TGT CTT TCT GCC CTG ACA GT-3' and (*an/an*) F 5'-GC AAT

436   CAC TAA AAT GTC CGA TT-3', R 5'-TGT CTT TCT GCC CTG ACA GT-3'

437

438   ***4.2. Nissl staining and neocortical dimension analysis***

439   After dissection, brains were fixed in 4% PFA for overnight, dehydrated in an ethanol series

440   (50, 70, 85, 90, 100%), cleaned with xylene, and embedded in paraffin. 10 μm sections were

441   cut on a microtome and collected on Superfrost plus slides®. De-paraffinized coronal brain

442   sections at the level of corpus callosum and anterior commissure were incubated in 1% cresyl

443   violet (C5042, Sigma-Aldrich, USA) in acetate-buffered solution (pH 4.5) for 5 minutes. At the

444   level of corpus callosum and anterior commissure, parietal cortical thickness was measured

445   perpendicularly to pial surface, and neocortical area was estimated using ImageJ software.

446

447   ### *4.3. Golgi staining, dendritic complexity, and spine analysis*

448   Golgi-Cox impregnation of adult brain samples was performed as described (Zaqout and

449   Kaindl, 2016). Briefly, brains were immersed in the impregnation solution in darkness at room

450   temperature (RT) for 2 weeks, and transferred into tissue-protectant solution at 4 °C for 4 days.

451   Brains were cut into 200 µm sections for dendritic complexity analysis and 100 µm sections for

452   dendritic spine analysis as described previously (Schuster et al., 2015). Sections were collected

453   on gelatin-coated slides, left to dry for two days, developed, dehydrated through ethanol series,

454   cleared in xylol solution, and mounted in Eukitt (quick-252 hardening mounting medium; 03989,

455   Fluka analytical, Germany). For dendritic complexity assessment, Sholl analysis (SHOLL,

456   1953) was performed for layer 2/3 pyramidal neurons of matched +/+ and *an/an* somatosensory

457   neocortical regions. The total intersection number of the dendritic tree with 30 10-µm spaced

458   concentric circles were counted with cell counter plug-ins in ImageJ. Neurite tracer plug-in in

459   Fiji/ImageJ was used to draw representative neurons. The number of spines was counted in

460   20 µm long segments of secondary basal dendrites using ImageJ. Spines were classified to

461   one of three morphological subtypes: mushroom (short neck, large bulbous end), stubby (no

462   neck) and thin-shaped (long neck).

463

464   ### *4.4 Immunohistology and immunocytology*

465   Paraffin sections were deparaffinized, exposed to heat-mediated antigen retrieval citrate-based

466   solution (pH 6.0; H-3300, Vector Laboratories, USA), blocked for 1 hour with 10% donkey or

467   goat normal serum at RT, and incubated overnight with the primary antibody at RT followed by

468   an incubation with the corresponding secondary antibodies for 2 hours at RT. The following

469   primary antibodies were used at specified dilutions: rabbit anti-Cux1 (1:200; Santa Cruz

470   Biotechnology, Heidelberg, Germany, sc-13024 (Issa et al., 2013a)), rat anti-Ctip2 (1:250;

471   Abcam, Cambridge, UK, ab18465 (Issa et al., 2013a)), mouse anti-GABA (GABA, 1:100;

472   Chemicon, Temecula CA, MAB316 (Uematsu et al., 2008)), rabbit anti-NeuN (1:200; Merck-

473   Millipore, Germany, ABN78 (Issa et al., 2013a)), guinea pig anti-vesicular glutamate transporter

474   1 (VGlut1, 1:500; Merck-Millipore, Germany, AB5905 (Mitchell et al., 2012)), rabbit anti-

475   vesicular GABA transporter (VGat, 1:500; Merck-Millipore, Germany, AB5062P (Mitchell et al.,

476   2012)), and rabbit anti-post synaptic density 95 (PSD95, 1:200; Synaptic System, Göttingen,

477   Germany, 124-002 (Schuster et al., 2015)). Secondary antibodies were used at 1:400 dilution:

478   donkey Cy3-conjugated anti-rabbit and anti-mouse IgG (Jackson ImmunoResearch, Suffolk,

479   UK), donkey Alexa Fluor® 488 conjugate anti-rat, and anti-guinea pig IgG (Invitrogen,

480   Darmstadt, Germany). Nuclei were stained with 40,6-diamidino-2-phenylindole (DAPI, 1:1000,

481   Sigma-Aldrich, USA). Neuronal cultures were prepared from cortices of P0 – P2 +/+ and *an/an*

482   mice and stained with vesicular glutamate transporter 1 (VGlut1; excitatory presynaptic marker;

483   green) or vesicular GABA transporter (VGat; inhibitory presynaptic marker; red). Staining of

484   microtubule network with microtubule-associated protein Map2a (white) was used to display

485   soma and dendritic tree of individual neurons and count the number of cells per view field.

486   Cultures were fixed at DIV 14–16 with 4% PFA for 10 min and permeabilized with 1xPBS +

487   0.1% Tween 20 (PBS-T). Cells were blocked with PBS-T containing 5% donkey serum for 1 h,

488   before applying the primary antibody overnight at 4°C (anti-Map2a, Millipore, anti-VGlut1 and

489   anti-VGat, Synaptic Systems). The secondary fluorophore-conjugated antibody was incubated

490   for 1 h at RT. All antibodies used in this paper are well established and were previously applied

491   by others and us on mouse tissue. In addition, negative control staining experiments including

492   the application of the secondary antibody only have been performed (Fig S1).

493

494   ***4.5 Electrophysiology on ex-vivo brain slices***

495   Slices of mouse brains (P6/7 and adult) were used for *ex-vivo* recordings. Mice were

496   decapitated, brains removed, and transferred to ice-cold artificial cerebrospinal fluid (ACSF)

497   containing 85 mM NaCl, 26 mM NaHCO$_3$, 2.5 mM KCl, 1 mM NaH$_2$PO$_4$, 0.5 mM CaCl$_2$, 7 mM

498   MgCl$_2$, 50 mM sucrose, and 10 mM glucose (290-310 mOsm). Coronal slices (300 µm thick)

499   containing somatosensory cortex were cut on a Leica VT1200S (Leica Microsystems,

500   Germany). Slices recovered for 30 minutes at 34 °C and were kept at room temperature

501   afterwards. Somatic whole-cell recordings were performed in a submerged recording chamber

502 perfused with ACSF containing 117 mM NaCl, 3.5 mM KCl, 1.25 mM NaH_2PO4, 2 mM $MgSO_4$

503 or $MgCl_2$, 26 mM NaHCO3, 10 mM glucose, and 2 mM $CaCl_2$. All ACSF solutions were

504 constantly gassed with 95% O_2/5% CO_2, osmolarity was between 290 and 305 mosmol/l, and

505 experiments were performed at 32-34 °C. Pyramidal neurons were visually identified in layer

506 2/3 using an upright microscope equipped with infrared differential interference contrast optics

507 (Axioskop FS2; Zeiss or Olympus BX51, Germany). Whole-cell patch clamp recordings were

508 conducted with pipettes (tip resistance 3-5 MΩ) filled with intracellular solution containing 120

509 mM K-gluconate, 10 mM KCl, 10 mM Na-phosphocreatine, 1 mM $MgCl_2$, 1 mM $CaCl_2$, 11 mM

510 EGTA, 10 mM HEPES, 2 mM Mg_2+-ATP, 0.3 mM Tris-GTP (pH 7.25, 288 mOsm). Only

511 neurons with resting potentials below –65 mV and spiking characteristics of pyramidal neurons

512 were included in the analysis. Input resistance was calculated with a linear fit of the current

513 clamp generated I-V plot in close vicinity of the resting potential. Intersection of the linear

514 regression of the F-I relationship (estimated in the linear range) and abscissa roughly

515 approximated the rheobase. Postsynaptic currents were recorded in voltage clamp at a holding

516 potential of –60 mV. Under these conditions, most spontaneous postsynaptic events are

517 mediated by activation of glutamatergic, AMPA receptor mediated currents (Schuster et al.,

518 2015). Miniature postsynaptic currents (mPSCs) were recorded in the presence of 0.5-1 µM

519 tetrodotoxin (TTX). mEPSCs were analyzed in presence of bicuculline (20 µM) while mIPSC

520 were analyzed in presence of 10 µM CNQX and 25 µM D-AP5 and with KCl-based internal

521 solutions (all Tocris Bioscience). Data from patch-clamp recordings were collected with an

522 EPC-10 double amplifier (HEKA, Germany), digitized (10 kHz, after Bessel filtering at 2.9 kHz),

523 and stored using PatchMaster software (HEKA). Series resistance (R_S) was monitored

524 throughout experiments; neurons were rejected if R_S was > 20 MΩ or varied > ± 30%. No R_S

525 compensation was used. Liquid junction potentials were not corrected for. Synaptic events

526 were detected offline using the Mini Analysis Program (Synaptosoft Inc., USA) and a threshold

527 of 3.5 times noise (standard deviation of regions without manually detectable postsynaptic

528 currents). All events were visually counterchecked. As integrated measure the total charge

529 transfer was calculated from the equation: $Q = f \times Q_{PSCs}$, where f is the frequency (s^{-1}), and

530 Q_{PSCs} is the average charge transfer for each PSC (Ataka and Gu, 2006). Paired EPSCs (50

531 ms interval) were elicited by square pulse (100 µs) stimulation of the slice 50–100 µm lateral

532 of the recording electrode at the border between layer 2/3 and 4 with a concentric tungsten

533 electrode (TM33CCINS, WPI, USA). All compounds used were purchased from Sigma-Aldrich,

534 Germany unless stated otherwise.

535

536 ***4.6. Electrophysiology on dissociated cell cultures***

537 Autaptic and continental primary neuronal cultures from the cortices were prepared from

538 newborn (P0-P2) mice, and neurons were plated on astrocyte feeder layer from cortices of non-

539 mutated *C57/Bl6* mouse pups (P0-P2; prepared 2 weeks before plating the neurons) as

540 previously described (Wu et al., 2015). Briefly, cortices were removed, enzymatically and

541 mechanically dissociated. Neurons were cultured in Neurobasal-A media containing B-27

542 Supplement, 10 IU/ml penicillin, 1 g/ml streptomycin, and 2 mM L-alanyl-L-glutamine. The

543 seeding density for continental cultures was 1.35×10^4 cells/cm^2. Cultures with different

544 genotypes were generated from siblings that were treated identically during culturing and

545 incubated at 37 °C with 5% CO_2. Whole cell voltage-clamp recordings from autaptic cortical

546 excitatory neurons were obtained between *days in vitro* (DIV) 14-16 at RT. Recordings and

547 analysis of data were done as previously described (Wu et al., 2015). Extracellular solution

548 contained in mM: 140 NaCl, 2.4 KCl, 10 HEPES, 10 glucose, 2 $CaCl_2$, and 4 $MgCl_2$. The pipette

549 internal solution contained in mM: 136 KCl, 17.8 HEPES, 1 EGTA, 4.6 $MgCl_2$, 4 ATP-Na_2, 0.3

550 GTP-Na_2, 12 creatine phosphate, and 50 U/ml phosphocreatine kinase. Both extracellular and

551 internal solutions were adjusted to pH 7.4 and osmolarity of ~300 mOsm. Borosilicate glass

552 pipettes had a resistance of 3–4 MΩ. Recordings were performed with a MultiClamp 700B

553 amplifier, and data were acquired with Clampex 10.0 (Molecular Devices). To verify

554 glutamatergic responses in autaptic cultures, 3 mM kynurenic acid was applied to the

555 extracellular solution. Sucrose solution (500 mM added to external solution) was applied for 5

556 s to assess the size of the readily releasable pool (RRP; (Rosenmund and Stevens, 1996)).

557 Evoked EPSCs were recorded after somatic depolarization from –70 to 0 mV for 2 ms.

558 Vesicular release probability (*Pvr*) was determined by calculating the EPSC charge divided by

559 the RRP charge of individual neurons. Spontaneous release was determined as mEPSC and

560 was recorded for 60 s at –70 mV. To subtract background noise, recording was performed with

561 the application of 3 mM kynurenic acid for the same duration. Traces were filtered at 1 kHz,

and events were detected by using a template-based algorithm in AxoGraphX. Data was collected from two independent cultures.

4.7. Imaging

Brightfield images of Nissl-stained brain sections and Golgi-stained dendritic spines were taken by Olympus BX60 microscope equipped with an Axiocam MRc Zeiss camera and Axiovision 4.8 software (Zeiss, Göttingen, Germany). For studying dendritic arborization, 1-µm-spaced Z-stack brightfield images were taken by an Olympus IX81 microscope equipped with an F View II (sw) camera (Soft Imaging System GmbH, Münster, Germany). Fluorescent images of layer markers were taken by Olympus BX51 microscope by an Intas camera and Magnafire 2.1B software (Olympus, Hamburg, Germany). Fluorescent images of synaptic markers were taken by an lsm5exciter Zeiss confocal microscope with the software Zen (version 2009, Zeiss, Jena, Germany). Fluorescent images of dissociated cell culture were taken with an Olympus IX81 epifluorescent microscope. All images were processed using Adobe Photoshop CS6 version 13.0x64 and Fiji/ImageJ software.

4.8. Statistical analysis

For *in-vivo* parietal cortical thickness, neocortical area, cortical layers, Scholl analysis, and spine density statistics, two-tailed Student's t-tests (TT) were applied. Statistics of *ex-vivo* brain slices electrophysiology were performed using Origin8.5 (OriginLab, USA). For normally distributed datasets (Shapiro-Wilk test) TT was used. In the case of significant deviations from normal distribution ($p \leq 0.05$) the non-parametric Mann-Whitney-U test (MWU) was used. The frequency of mEPSCs before and after application of bicuculline was analyzed with two way repeated measures ANOVA and *post hoc* Bonferroni multiple-comparison tests (ANOVA-RM-B). Data of dissociated cell cultures were first tested for a Gaussian distribution with D'Agostino and Pearson omnibus normality test. If data were normally distributed, one-way ANOVA followed by Bonferroni multiple-comparison tests were performed. Otherwise, nonparametric Kruskal-Wallis test followed by Dunn multiple comparison tests were used.

Authors' contributions

AMK, US, and CR were responsible for project conception. AMK, SZ, KB and US wrote the manuscript. SZ, KB, YJW, SO, US, LLB, MR and NK performed and analyzed the experiments. All authors read, revised, and approved the final manuscript.

Acknowledgments

Conflicts of Interest

The authors declare that they have no competing interests.

References

Ataka, T., Gu, J.G., 2006. Relationship between tonic inhibitory currents and phasic inhibitory activity in the spinal cord lamina II region of adult mice. Mol Pain 2, 36. doi:10.1186/1744-8069-2-36

Barrera, J.A., Kao, L.-R., Hammer, R.E., Seemann, J., Fuchs, J.L., Megraw, T.L., 2010. CDK5RAP2 regulates centriole engagement and cohesion in mice. Dev. Cell 18, 913–926. doi:10.1016/j.devcel.2010.05.017

Bartolini, G., Ciceri, G., Marín, O., 2013. Integration of GABAergic interneurons into cortical cell assemblies: lessons from embryos and adults. Neuron 79, 849–864. doi:10.1016/j.neuron.2013.08.014

Bond, J., Roberts, E., Springell, K., Lizarraga, S.B., Lizarraga, S., Scott, S., Higgins, J., Hampshire, D.J., Morrison, E.E., Leal, G.F., Silva, E.O., Costa, S.M.R., Baralle, D., Raponi, M., Karbani, G., Rashid, Y., Jafri, H., Bennett, C., Corry, P., Walsh, C.A., Woods, C.G., 2005. A centrosomal mechanism involving CDK5RAP2 and CENPJ controls brain size. Nat Genet 37, 353–355. doi:10.1038/ng1539

Bortone, D., Polleux, F., 2009. KCC2 expression promotes the termination of cortical interneuron migration in a voltage-sensitive calcium-dependent manner. Neuron 62, 53–71. doi:10.1016/j.neuron.2009.01.034

Buchman, J.J., Tseng, H.-C., Zhou, Y., Frank, C.L., Xie, Z., Tsai, L.-H., 2010. Cdk5rap2 interacts with pericentrin to maintain the neural progenitor pool in the developing neocortex. Neuron 66, 386–402. doi:10.1016/j.neuron.2010.03.036

Buhl, E.H., Halasy, K., Somogyi, P., 1994. Diverse sources of hippocampal unitary inhibitory postsynaptic potentials and the number of synaptic release sites. Nature 368, 823–828. doi:10.1038/368823a0

Chattopadhyaya, B., Di Cristo, G., Higashiyama, H., Knott, G.W., Kuhlman, S.J., Welker, E., Huang, Z.J., 2004. Experience and activity-dependent maturation of perisomatic GABAergic innervation in primary visual cortex during a postnatal critical period. Journal of Neuroscience 24, 9598–9611. doi:10.1523/JNEUROSCI.1851-04.2004

Chung, D.W., Wills, Z.P., Fish, K.N., Lewis, D.A., 2017. Developmental pruning of excitatory synaptic inputs to parvalbumin interneurons in monkey prefrontal cortex. Proc Natl Acad Sci USA 114, E629–E637. doi:10.1073/pnas.1610077114

Cossart, R., 2011. The maturation of cortical interneuron diversity: how multiple developmental journeys shape the emergence of proper network function. Curr Opin Neurobiol 21, 160–168. doi:10.1016/j.conb.2010.10.003

Dailey, M.E., Smith, S.J., 1996. The Dynamics of Dendritic Structure in Developing Hippocampal Slices. J Neurosci 16, 2983–2994.

del CASTILLO, J., KATZ, B., 1954. Quantal components of the end-plate potential. The Journal of Physiology 124, 560–573.

DiStasio, A., Driver, A., Sund, K., Donlin, M., Muraleedharan, R.M., Pooya, S., Kline-Fath, B., Kaufman, K.M., Prows, C.A., Schorry, E., Dasgupta, B., Stottmann, R.W., 2017. Copb2 is essential for embryogenesis and hypomorphic mutations cause human microcephaly. Hum. Mol. Genet. 26, 4836–4848. doi:10.1093/hmg/ddx362

Draguhn, A., Buzsáki, G., 2004. Neuronal oscillations in cortical networks. Science 304, 1926–1929. doi:10.1126/science.1099745

Fish, J.L., Kosodo, Y., Enard, W., Pääbo, S., Huttner, W.B., 2006. Aspm specifically maintains symmetric proliferative divisions of neuroepithelial cells. Proc Natl Acad Sci USA 103, 10438–10443. doi:10.1073/pnas.0604066103

Flores, C.E., Nikonenko, I., Mendez, P., Fritschy, J.-M., Tyagarajan, S.K., Muller, D., 2015. Activity-dependent inhibitory synapse remodeling through gephyrin phosphorylation. Proc Natl Acad Sci USA 112, E65–72. doi:10.1073/pnas.1411170112

Fong, K.-W., Choi, Y.-K., Rattner, J.B., Qi, R.Z., 2008. CDK5RAP2 is a pericentriolar protein that functions in centrosomal attachment of the gamma-tubulin ring complex. Mol Biol Cell 19, 115–125. doi:10.1091/mbc.E07-04-0371

Guo, J., Anton, E.S., 2014. Decision making during interneuron migration in the developing cerebral cortex. Trends Cell Biol. 24, 342–351. doi:10.1016/j.tcb.2013.12.001

Hassan, M.J., Khurshid, M., Azeem, Z., John, P., Ali, G., Chishti, M.S., Ahmad, W., 2007. Previously described sequence variant in CDK5RAP2 gene in a Pakistani family with autosomal recessive primary microcephaly. BMC Med. Genet. 8, 58. doi:10.1186/1471-2350-8-58

House, D.R.C., Elstrott, J., Koh, E., Chung, J., Feldman, D.E., 2011. Parallel regulation of feedforward inhibition and excitation during whisker map plasticity. Neuron 72, 819–831. doi:10.1016/j.neuron.2011.09.008

Isaacson, J.S., Scanziani, M., 2011. How inhibition shapes cortical activity. Neuron 72, 231–243. doi:10.1016/j.neuron.2011.09.027

Issa, L., Kraemer, N., Rickert, C.H., Sifringer, M., Ninnemann, O., Stoltenburg-Didinger, G., Kaindl, A.M., 2013a. CDK5RAP2 expression during murine and human brain development correlates with pathology in primary autosomal recessive microcephaly. Cereb Cortex 23, 2245–2260. doi:10.1093/cercor/bhs212

Issa, L., Mueller, K., Seufert, K., Kraemer, N., Rosenkotter, H., Ninnemann, O., Buob, M., Kaindl, A.M., Morris-Rosendahl, D.J., 2013b. Clinical and cellular features in patients with primary autosomal recessive microcephaly and a novel CDK5RAP2 mutation. Orphanet J Rare Dis 8, 59. doi:10.1186/1750-1172-8-59

Jiao, Y., Zhang, C., Yanagawa, Y., Sun, Q.-Q., 2006. Major effects of sensory experiences on the neocortical inhibitory circuits. Journal of Neuroscience 26, 8691–8701. doi:10.1523/JNEUROSCI.2478-06.2006

Kadir, R., Harel, T., Markus, B., Perez, Y., Bakhrat, A., Cohen, I., Volodarsky, M., Feintsein-Linial, M., Chervinski, E., Zlotogora, J., Sivan, S., Birnbaum, R.Y., Abdu, U., Shalev, S., Birk, O.S., 2016. ALFY-Controlled DVL3 Autophagy Regulates Wnt Signaling, Determining Human Brain Size. PLoS Genet 12, e1005919. doi:10.1371/journal.pgen.1005919

Kaindl, A.M., Passemard, S., Kumar, P., Kraemer, N., Issa, L., Zwirner, A., Gerard, B., Verloes, A., Mani, S., Gressens, P., 2010. Many roads lead to primary autosomal recessive microcephaly. Prog Neurobiol 90, 363–383. doi:10.1016/j.pneurobio.2009.11.002

Kepecs, A., Fishell, G., 2014. Interneuron cell types are fit to function. Nature 505, 318–326. doi:10.1038/nature12983

Kilb, W., 2012. Development of the GABAergic system from birth to adolescence. Neuroscientist 18, 613–630. doi:10.1177/1073858411422114

Kim, A.H., Puram, S.V., Bilimoria, P.M., Ikeuchi, Y., Keough, S., Wong, M., Rowitch, D., Bonni, A., 2009. A centrosomal Cdc20-APC pathway controls dendrite morphogenesis in postmitotic neurons. Cell 136, 322–336. doi:10.1016/j.cell.2008.11.050

Kraemer, N., Issa, L., Hauck, S.C.R., Mani, S., Ninnemann, O., Kaindl, A.M., 2011. What's the hype about CDK5RAP2? Cell Mol Life Sci 68, 1719–1736. doi:10.1007/s00018-011-0635-4

Kraemer, N., Ravindran, E., Zaqout, S., Neubert, G., Schindler, D., Ninnemann, O., Gräf, R., Seiler, A.E.M., Kaindl, A.M., 2015. Loss of CDK5RAP2 affects neural but not non-neural mESC differentiation into cardiomyocytes. Cell Cycle 14, 2044–2057. doi:10.1080/15384101.2015.1044169

Lazarus, M.S., Huang, Z.J., 2011. Distinct maturation profiles of perisomatic and dendritic targeting GABAergic interneurons in the mouse primary visual cortex during the critical period of ocular dominance plasticity. J Neurophysiol 106, 775–787. doi:10.1152/jn.00729.2010

Lim, L., Mi, D., Llorca, A., Marín, O., 2018. Development and Functional Diversification of Cortical Interneurons. Neuron 100, 294–313. doi:10.1016/j.neuron.2018.10.009

Lin, Y., Bloodgood, B.L., Hauser, J.L., Lapan, A.D., Koon, A.C., Kim, T.-K., Hu, L.S., Malik, A.N., Greenberg, M.E., 2008. Activity-dependent regulation of inhibitory synapse development by Npas4. Nature 455, 1198–1204. doi:10.1038/nature07319

Lizarraga, S.B., Margossian, S.P., Harris, M.H., Campagna, D.R., Han, A.-P., Blevins, S., Mudbhary, R., Barker, J.E., Walsh, C.A., Fleming, M.D., 2010. Cdk5rap2 regulates centrosome function and chromosome segregation in neuronal progenitors. Development 137, 1907–1917. doi:10.1242/dev.040410

López Bendito, G., Luján, R., Shigemoto, R., Ganter, P., Paulsen, O., Molnár, Z., 2003. Blockade of GABA(B) receptors alters the tangential migration of cortical neurons. Cereb Cortex 13, 932–942.

Luhmann, H.J., Prince, D.A., 1991. Postnatal maturation of the GABAergic system in rat neocortex. J Neurophysiol 65, 247–263. doi:10.1152/jn.1991.65.2.247

Maric, D., Liu, Q.Y., Maric, I., Chaudry, S., Chang, Y.H., Smith, S.V., Sieghart, W., Fritschy, J.M., Barker, J.L., 2001. GABA expression dominates neuronal lineage progression in the embryonic rat neocortex and facilitates neurite outgrowth via GABA(A) autoreceptor/Cl- channels. Journal of Neuroscience 21, 2343–2360.

Marín, O., 2012. Interneuron dysfunction in psychiatric disorders. Nature Publishing Group 13, 107–120. doi:10.1038/nrn3155

Matsuzaki, M., Ellis-Davies, G.C., Nemoto, T., Miyashita, Y., Iino, M., Kasai, H., 2001. Dendritic spine geometry is critical for AMPA receptor expression in hippocampal CA1 pyramidal neurons. Nat Neurosci 4, 1086–1092. doi:10.1038/nn736

Mitchell, N., Petralia, R.S., Currier, D.G., Wang, Y.-X., Kim, A., Mattson, M.P., Yao, P.J., 2012. Sonic hedgehog regulates presynaptic terminal size, ultrastructure and function in hippocampal neurons. Journal of Cell Science 125, 4207–4213. doi:10.1242/jcs.105080

Moawia, A., Shaheen, R., Rasool, S., Waseem, S.S., Ewida, N., Budde, B., Kawalia, A., Motameny, S., Khan, K., Fatima, A., Jameel, M., Ullah, F., Akram, T., Ali, Z., Abdullah, U., Irshad, S., Höhne, W., Noegel, A.A., Al-Owain, M., Hörtnagel, K., Stöbe, P., Baig, S.M., Nürnberg, P., Alkuraya, F.S., Hahn, A., Hussain, M.S., 2017. Mutations of KIF14 cause primary microcephaly by impairing cytokinesis. Ann. Neurol. 82, 562–577. doi:10.1002/ana.25044

Nair, D., Hosy, E., Petersen, J.D., Constals, A., Giannone, G., Choquet, D., Sibarita, J.-B., 2013. Super-resolution imaging reveals that AMPA receptors inside synapses are dynamically organized in nanodomains regulated by PSD95. Journal of Neuroscience 33, 13204–13224. doi:10.1523/JNEUROSCI.2381-12.2013

Nelson, S.B., Valakh, V., 2015. Excitatory/Inhibitory Balance and Circuit Homeostasis in Autism Spectrum Disorders. Neuron 87, 684–698. doi:10.1016/j.neuron.2015.07.033

Oh, W.C., Lutzu, S., Castillo, P.E., Kwon, H.-B., 2016. De novo synaptogenesis induced by GABA in the developing mouse cortex. Science 353, 1037–1040. doi:10.1126/science.aaf5206

Pangratz-Fuehrer, S., Hestrin, S., 2011. Synaptogenesis of electrical and GABAergic

753   synapses of fast-spiking inhibitory neurons in the neocortex. Journal of Neuroscience 31,
754   10767–10775. doi:10.1523/JNEUROSCI.6655-10.2011
755 Passemard, S., Titomanlio, L., Elmaleh, M., Afenjar, A., Alessandri, J.-L., Andria, G., de
756   Villemeur, T.B., Boespflug-Tanguy, O., Burglen, L., Del Giudice, E., Guimiot, F., Hyon,
757   C., Isidor, B., Mégarbané, A., Moog, U., Odent, S., Hernandez, K., Pouvreau, N., Scala,
758   I., Schaer, M., Gressens, P., Gerard, B., Verloes, A., 2009. Expanding the clinical and
759   neuroradiologic phenotype of primary microcephaly due to ASPM mutations. Neurology
760   73, 962–969. doi:10.1212/WNL.0b013e3181b8799a
761 Pouille, F., Scanziani, M., 2001. Enforcement of temporal fidelity in pyramidal cells by somatic
762   feed-forward inhibition. Science 293, 1159–1163. doi:10.1126/science.1060342
763 Prange, O., Wong, T.P., Gerrow, K., Wang, Y.T., El-Husseini, A., 2004. A balance between
764   excitatory and inhibitory synapses is controlled by PSD-95 and neuroligin. Proc Natl
765   Acad Sci USA 101, 13915–13920. doi:10.1073/pnas.0405939101
766 Rico, B., Marín, O., 2011. Neuregulin signaling, cortical circuitry development and
767   schizophrenia. Curr. Opin. Genet. Dev. 21, 262–270. doi:10.1016/j.gde.2010.12.010
768 Rosenmund, C., Stevens, C.F., 1996. Definition of the readily releasable pool of vesicles at
769   hippocampal synapses. Neuron 16, 1197–1207.
770 Rudy, B., Fishell, G., Lee, S., Hjerling-Leffler, J., 2011. Three groups of interneurons account
771   for nearly 100% of neocortical GABAergic neurons. Dev Neurobiol 71, 45–61.
772   doi:10.1002/dneu.20853
773 Schuster, S., Rivalan, M., Strauss, U., Stoenica, L., Trimbuch, T., Rademacher, N.,
774   Parthasarathy, S., Lajkó, D., Rosenmund, C., Shoichet, S.A., Winter, Y., Tarabykin, V.,
775   Rosário, M., 2015. NOMA-GAP/ARHGAP33 regulates synapse development and
776   autistic-like behavior in the mouse. Mol. Psychiatry 20, 1120–1131.
777   doi:10.1038/mp.2015.42
778 SHOLL, D.A., 1953. Dendritic organization in the neurons of the visual and motor cortices of
779   the cat. J Anat 87, 387–406.
780 Silva, C.G., Peyre, E., Adhikari, M.H., Tielens, S., Tanco, S., Van Damme, P., Magno, L.,
781   Krusy, N., Agirman, G., Magiera, M.M., Kessaris, N., Malgrange, B., Andrieux, A., Janke,
782   C., Nguyen, L., 2018. Cell-Intrinsic Control of Interneuron Migration Drives Cortical
783   Morphogenesis. Cell 172, 1063–1078.e19. doi:10.1016/j.cell.2018.01.031
784 Soltesz, I., Smetters, D.K., Mody, I., 1995. Tonic inhibition originates from synapses close to
785   the soma. Neuron 14, 1273–1283.
786 Spruston, N., Jaffe, D.B., Williams, S.H., Johnston, D., 1993. Voltage- and space-clamp
787   errors associated with the measurement of electrotonically remote synaptic events. J
788   Neurophysiol 70, 781–802. doi:10.1152/jn.1993.70.2.781
789 Takesian, A.E., Hensch, T.K., 2013. Balancing plasticity/stability across brain development.
790   Prog Brain Res 207, 3–34. doi:10.1016/B978-0-444-63327-9.00001-1
791 Tuncdemir, S.N., Wamsley, B., Stam, F.J., Osakada, F., Goulding, M., Callaway, E.M., Rudy,
792   B., Fishell, G., 2016. Early Somatostatin Interneuron Connectivity Mediates the
793   Maturation of Deep Layer Cortical Circuits. Neuron 89, 521–535.
794   doi:10.1016/j.neuron.2015.11.020
795 Turrigiano, G., Leslie, K.R., Desai, N.S., Rutherford, L.C., Nelson, S.B., 1998. Activity-
796   dependent scaling of quantal amplitude in neocortical neurons. Nature 391, 892–896.
797   doi:10.1038/36103
798 Uematsu, M., Hirai, Y., Karube, F., Ebihara, S., Kato, M., Abe, K., Obata, K., Yoshida, S.,
799   Hirabayashi, M., Yanagawa, Y., Kawaguchi, Y., 2008. Quantitative chemical composition
800   of cortical GABAergic neurons revealed in transgenic venus-expressing rats. Cereb
801   Cortex 18, 315–330. doi:10.1093/cercor/bhm056
802 Wang, D.D., Kriegstein, A.R., 2009. Defining the role of GABA in cortical development. The
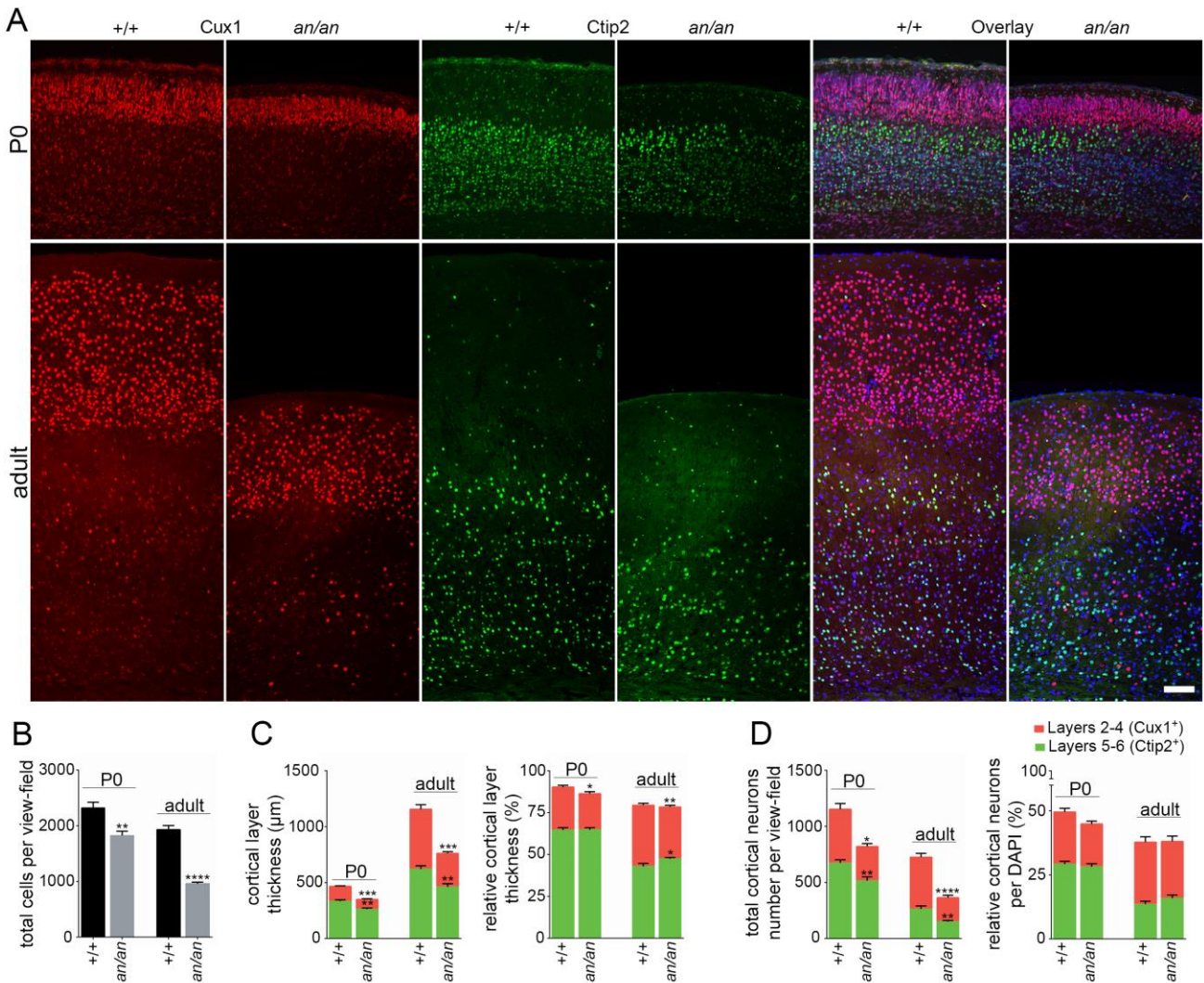803   Journal of Physiology 587, 1873–1879. doi:10.1113/jphysiol.2008.167635
804 Wang, D.D., Kriegstein, A.R., 2008. GABA regulates excitatory synapse formation in the
805   neocortex via NMDA receptor activation. Journal of Neuroscience 28, 5547–5558.
806   doi:10.1523/JNEUROSCI.5599-07.2008
807 Wu, Y.-J., Tejero, R., Arancillo, M., Vardar, G., Korotkova, T., Kintscher, M., Schmitz, D.,
808   Ponomarenko, A., Tabares, L., Rosenmund, C., 2015. Syntaxin 1B is important for
809   mouse postnatal survival and proper synaptic function at the mouse neuromuscular
810   junctions. J Neurophysiol 114, 2404–2417. doi:10.1152/jn.00577.2015
811 Xiang, Z., Huguenard, J.R., Prince, D.A., 1998. Cholinergic switching within neocortical
812   inhibitory networks. Science 281, 985–988.

813   Xue, M., Atallah, B.V., Scanziani, M., 2014. Equalizing excitation-inhibition ratios across
814   visual cortical neurons. Nature 511, 596–600. doi:10.1038/nature13321
815   Yoon, B.-E., Lee, C.J., 2014. GABA as a rising gliotransmitter. Front Neural Circuits 8, 141.
816   doi:10.3389/fncir.2014.00141
817   Zaqout, S., Bessa, P., Krämer, N., Stoltenburg-Didinger, G., Kaindl, A.M., 2017a. CDK5RAP2
818   Is Required to Maintain the Germ Cell Pool during Embryonic Development. Stem Cell
819   Reports 8, 198–204. doi:10.1016/j.stemcr.2017.01.002
820   Zaqout, S., Kaindl, A.M., 2016. Golgi-Cox Staining Step by Step. Frontiers in neuroanatomy
821   10, 38. doi:10.3389/fnana.2016.00038
822   Zaqout, S., Morris-Rosendahl, D., Kaindl, A.M., 2017b. Autosomal Recessive Primary
823   Microcephaly (MCPH): An Update. Neuropediatrics 48, 135–142. doi:10.1055/s-0037-
824   1601448
825   Zhang, X., Liu, D., Lv, S., Wang, H., Zhong, X., Liu, B., Wang, B., Liao, J., Li, J., Pfeifer, G.P.,
826   Xu, X., 2009. CDK5RAP2 is required for spindle checkpoint function. Cell Cycle 8, 1206–
827   1216. doi:10.4161/cc.8.8.8205
828   Zhang, Z.-W., 2004. Maturation of layer V pyramidal neurons in the rat prefrontal cortex:
829   intrinsic properties and synaptic function. J Neurophysiol 91, 1171–1182.
830   doi:10.1152/jn.00855.2003

Figures and figure legends

Fig 1. Microcephaly with pronounced cortical thinning in *an/an* mice. (A) Coronal brain sections of P0 and adult littermate animals with parietal cortex sections magnified on the right side (Nissl staining, scale bars 500 µm). (B) Reduction of the neocortical area and parietal cortical thickness in *an/an* mice. Throughout these graphs n = 8 animals/group and error bars indicate S.E.M., TT, **$p < 0.01$, ****$p < 0.0001$. For age as additional between subject factor see ANOVA at table S1.

839

Fig 2. Preserved neocortical layer organization despite reduced thickness of upper cortical layers in *an/an* mice. (A) Coronal brain sections of P0 and adult littermate animals stained for upper layer marker Cux1 (layers 2-4) and deeper layer marker Ctip2 (layers 5-6) (immunofluorescence images, scale bar 100 μm). (B) Reduction of total DAPI+ nuclei per view-field in *an/an* mice. (C) While the Cux1+ upper layers and Ctip2+ deep layers are thinner, only the relative thickness of upper layers with respect to the total cortical thickness mice was reduced in *an/an* mice. The relative thickness of the deep layers with respect to the total cortical thickness was similar. (D) Reduction of the Cux1+ and Ctip2+ cortical layer neurons per view-field in *an/an* mice versus +/+ littermates without reduction in the relative number of both layers. Throughout these graphs n = 7 animals/group and error bars indicate S.E.M., TT, $p < 0.05$, **$p < 0.01$, ***$p < 0.001$, ****$p < 0.0001$. For age as additional between subject factor see ANOVA at table S1.

852
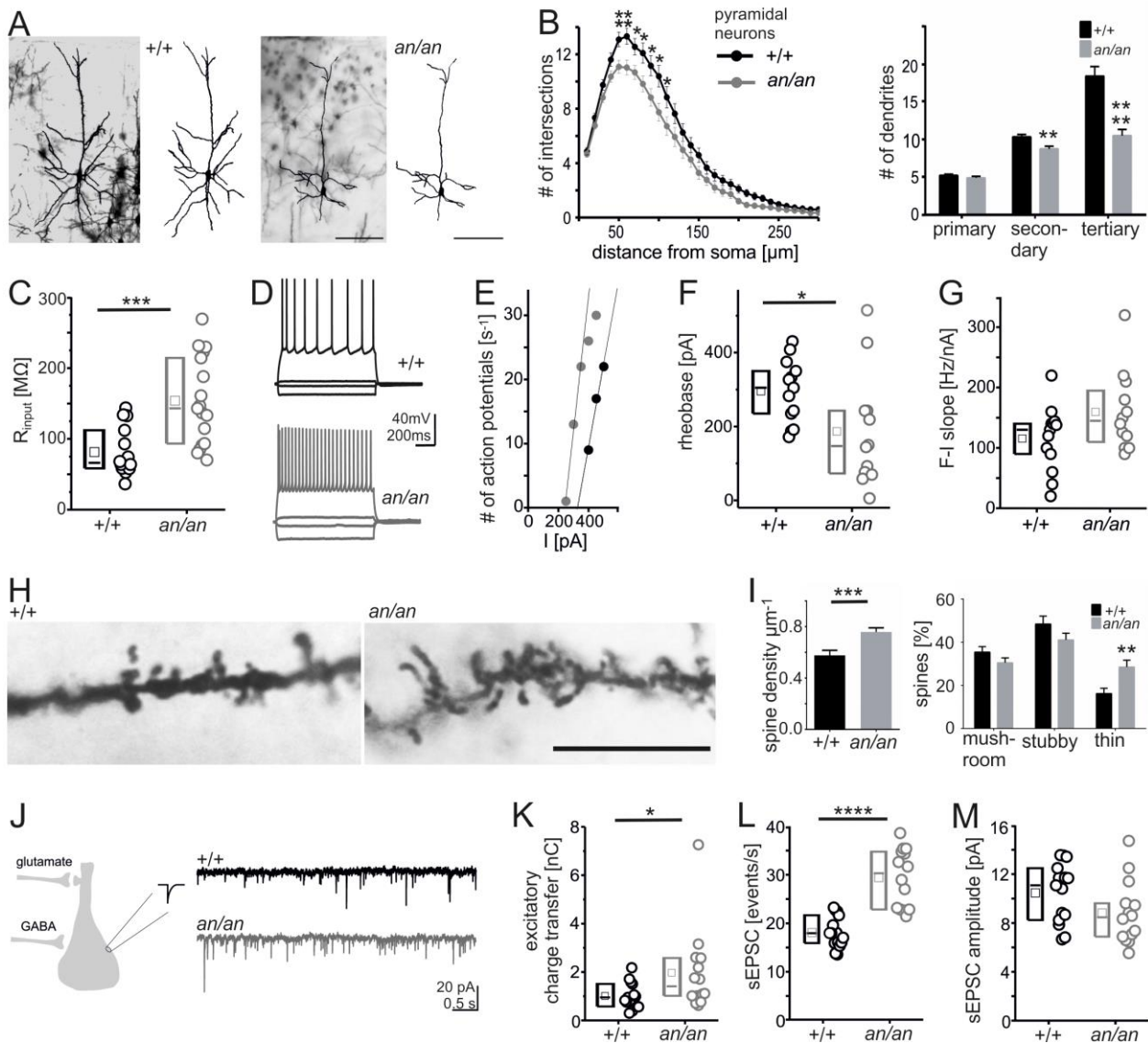
Fig 3. Distinctive morphological and physiological characteristics of layer 2/3 pyramidal

neurons from *an/an* mature neocortex. (A and B) Reduced dendritic complexity in

photomicrographs / reconstructed neurons (A, Golgi staining, scale bar 100 µm) as shown by

less dendritic intersections 50-110 µm from the soma and a reduction of the numbers of

secondary and tertiary dendrites in *an/an* mice (B, Sholl analysis, n = 44 +/+ and 39 *an/an*

neurons from 6 +/+ and 4 *an/an* animals). (C) Exemplary voltage responses to rectangular

current injections (-200, ±50 and 400 pA) depicting firing behavior (C) and the relation of elicited

action potentials and the current injected (D). (E and F) Population data showing shifted

neuronal offset (E) and a trend towards an increased gain in *an/an* neurons (F). (G) Input

resistance of *an/an* neurons was increased. (H) Magnified image of secondary basal dendrites

(Golgi staining, scale bar 10 µm). (I) Average spine density was increased (left) with a larger

864   proportion of thin-shaped immature spines in *an/an* mice (right, n = 410 +/+ and 373 *an/an*

865   spines counted in 34 (+/+) and 30 (*an/an*) 20 μm long dendritic segments from 5

866   animals/group). (J) Scheme and example traces of sEPSCs recordings in neurons voltage

867   clamped at -60mV. (K) Box plots showing an increased total excitatory charge transfer in *an/an*

868   mice due to increased sEPSCs frequency (L). (M) Average amplitudes were not altered. Serial

869   resistance ($R_{s+/+}$ = 9.8 ± 0.7 MΩ *vs.* $R_{san/an}$ = 11.0 ± 0.6 MΩ, p = 0.1; not shown) was

870   comparable. Population data for E-G and K-M are from 15 +/+ and 14 *an/an* neurons from 4

871   animals / group; age: P30 – P80). Boxes in this and the following figures represent 25-75%

872   plots, means and medians are depicted by an open square and a horizontal line, respectively.

873
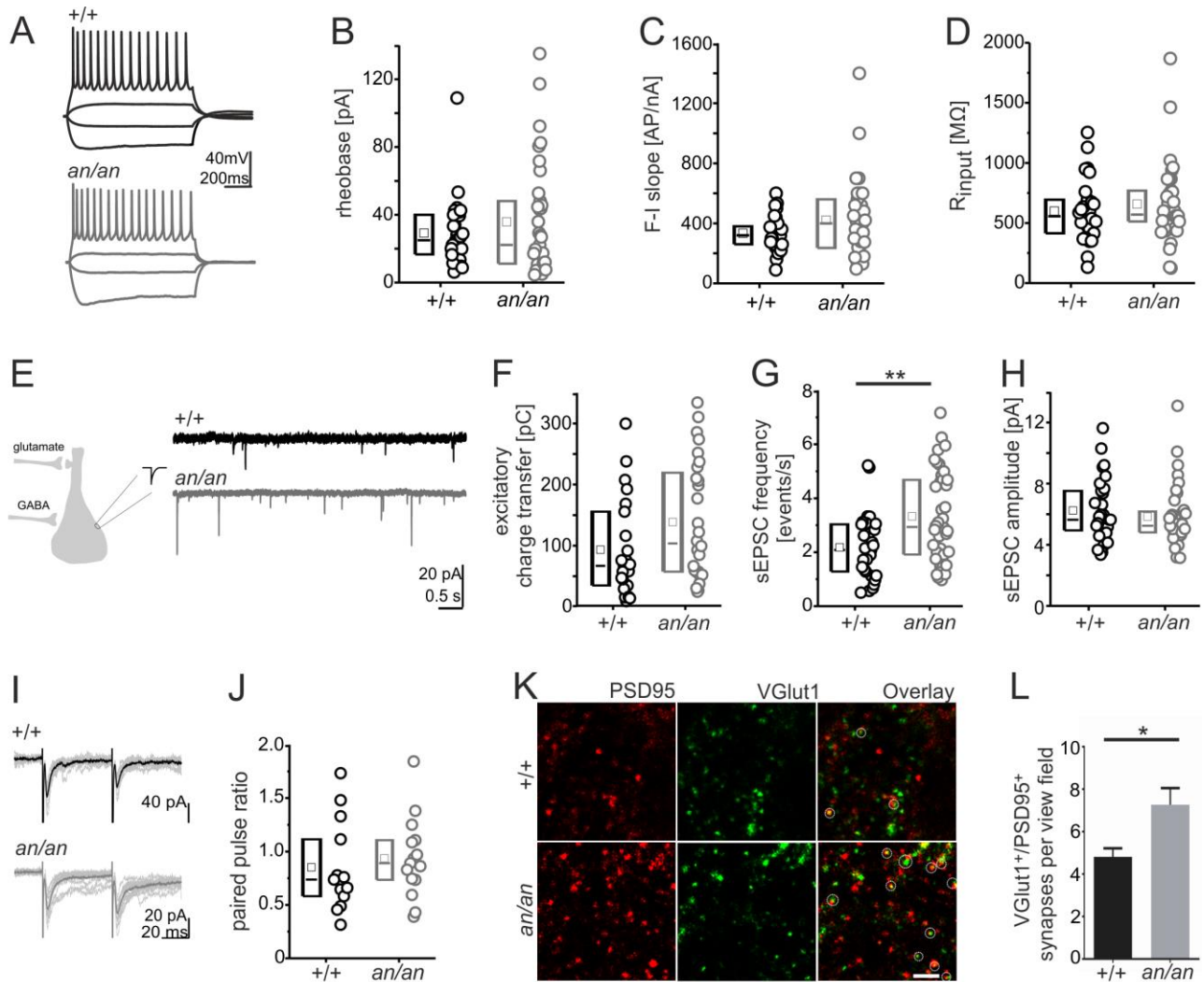
Fig 4. Increased excitatory synapse number and frequency of sEPSCs of layer 2/3 neocortical pyramidal neurons at onset of synaptogenesis (P6/7). (A) Voltage changes of exemplary +/+ (top) and *an/an* (bottom) neurons to rectangular current injections of -100, ± 25 and 100 pA. (B and C) Population data on neuronal offset (B) and gain (C) revealed no differences. (D) Input resistance did not vary between +/+ and *an/an* neurons. (E) Scheme and example traces for sEPSC recordings in neurons voltage clamped at -60mV. (F and G) Box plot graphs displaying values from 29 +/+ and 38 *an/an* neurons from 4 animals/group, showing a trend towards increased total excitatory charge transfer in *an/an* mice (F) and an increase in sEPSC frequency in neurons from *an/an* mice (G). (H) Average amplitudes remained unchanged. Serial resistance (Rs$_{+/+}$ = 9.1 ± 0.5 MΩ *vs.* Rs$_{an/an}$ = 8.8 ± 0.4 MΩ, p = 0.57; not shown) was similar. (I) Synaptic responses evoked by electrical stimulation overlay of 10 individual traces recorded with 20 sec intervals and a highlighted average trace. (J) population data of paired

886　　pulse ratio (PPR$_{+/+}$ = 0.85 ± 0.11 *vs.* PPR$_{an/an}$ = 0.93 ± 0.09, p = 0.6). (K) 100 µm^2 images of

887　　the upper layer of the parietal cortex at upper layer areas from littermate animals stained for

888　　VGlut1 (excitatory-presynaptic) and PSD95 (postsynaptic) markers. Overlay depicts

889　　VGlut1/PSD95 positive synapses (dotted circles) (confocal images, scale bar 2 µm). (L) The

890　　number of VGlut1/PSD95 positive synapses at layer 2/3 areas is increased in *an/an* mice (+/+

891　　= 4.8 ± 0.4 *vs. an/an* = 7.3 ± 0.8; n = 18 images from 4 +/+ animals and 28 images from 5 *an/an*

892　　animals).

894
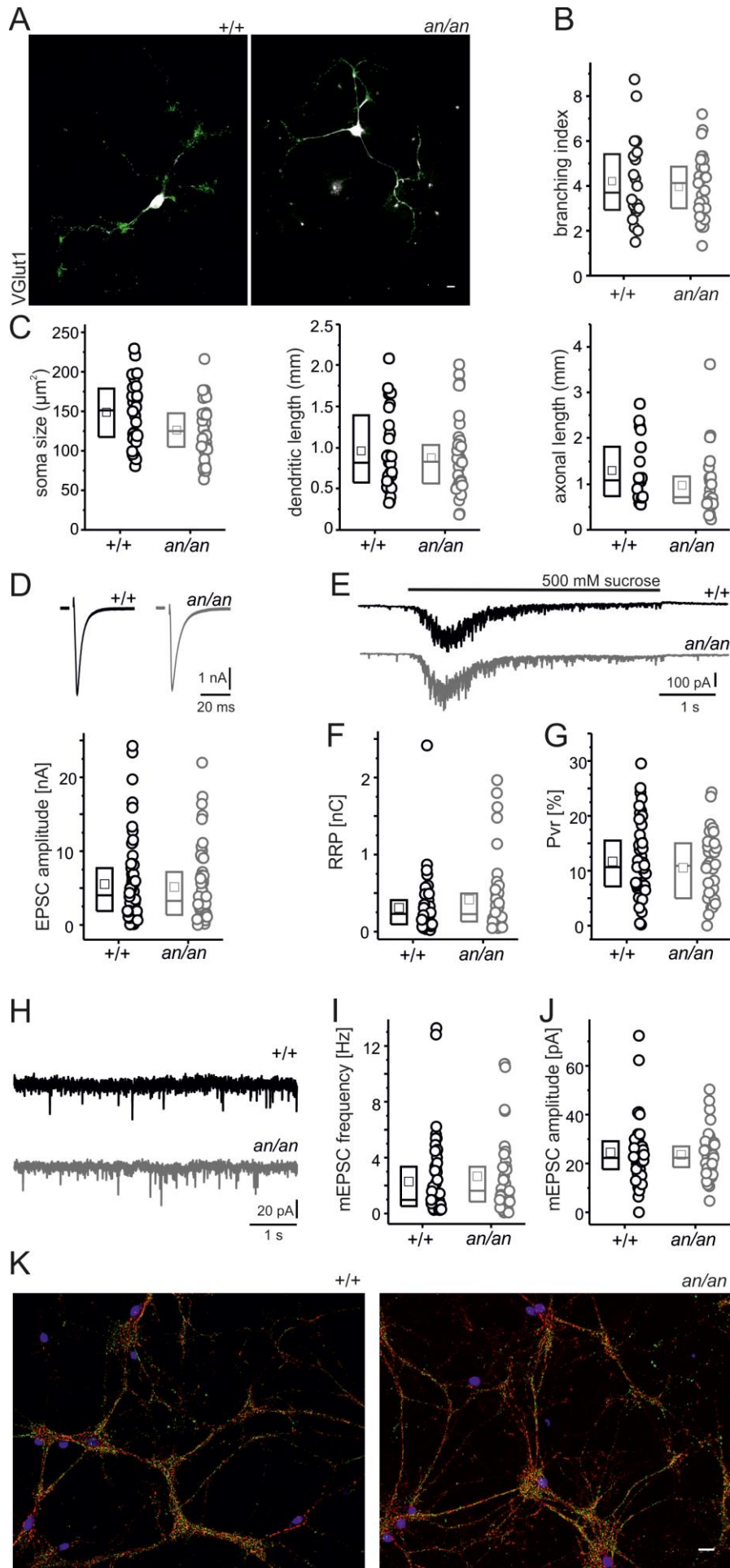
Fig 5. Neocortical pyramidal neurons derived from *an/an* and *+/+* mice display a comparable phenotype *in vitro*. (A) Photomicrographs of cultured neurons stained for neuronal cytoskeleton by microtubule associated protein (Map2 - white, all panels) and VGlut1 (green), scale bar: 10 µm. (B) Box plots of branching index estimated by the ratio of counts of dendritic tips / primary dendrites confirm a lack of alteration in branching patterns. (C) Box plots illustrating soma size, dendritic length and axonal length of autaptic cortical excitatory neurons. (D) Traces of excitatory postsynaptic currents (top) after a 2 ms depolarization (EPSC) and population data of EPSC amplitudes from 65 *+/+* (black) and 54 *an/an* (grey) autaptic cortical neurons. (E) Responses from *+/+* (black) and *an/an* (grey) cortical neurons during 500 mM sucrose application for 5 s. (F) Box plot of readily releasable pool (RRP) and (G) average vesicular release probability (P_{vr} = EPSC charge / RRP charge) in autaptic *+/+* (51) and *an/an* (44) cortical excitatory neurons. (H) Traces of mEPSC from *+/+* (black) and *an/an* (grey) neurons. (I and J) Box plots of mEPSC frequencies (I) and mEPSC amplitudes (J, *+/+*: 47 neurons; *an/an*: 43 neurons). Data was collected from 2 independent cultures. (K) Examples of continental (high density) cultures stained for presynaptic markers VGlut (green), VGat (red) and the nuclear marker DAPI (blue), scale bar: 25 µm.

911
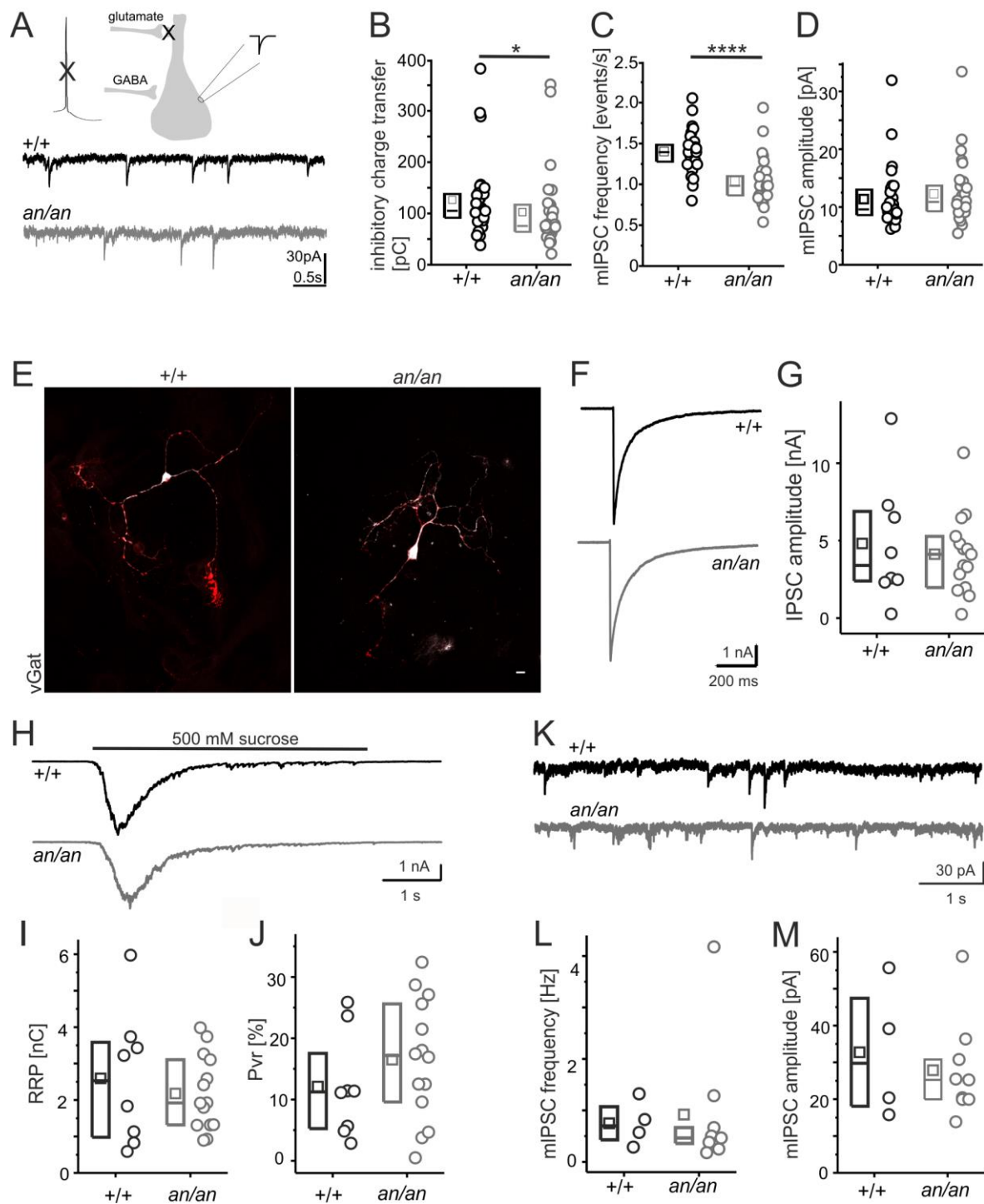
Fig 6. Decreased inhibition at the soma of layer 2/3 neocortical *ex-vivo* pyramidal neurons in P6/7 but not in cultured neurons from *an/an* mice. (A) Scheme and example of mIPSCs traces recorded at -60 mV using equimolar Cl⁻ and blocking excitatory postsynaptic currents with CNQX and DAP-5 (n = 30 +/+ and 32 *an/an* neurons from 3 animals/group). (B and C) Box plots showing a decreased total inhibitory charge transfer in *an/an* mice (B) due to reduced mIPSCs frequency in *an/an* neurons (C). (D) Box plot graph depicting the mean mIPSC

918   amplitudes shows no alteration between neurons from +/+ and *an/an* mice. Note that the slight

919   reduction in serial resistance of *an/an* cells ($R_{s+/+}$ = 11.6 ± 0.7 MΩ vs. $R_{san/an}$ = 9.3 ± 0.6 MΩ, p

920   = 0.009; not shown) might attenuate the difference in frequencies between the groups. (E)

921   Photomicrographs of autaptic inhibitory neurons stained for Map2 (white) and VGat (red), scale

922   bar: 10 μm. (F) Traces of inhibitory postsynaptic currents evoked by a 2 ms depolarization

923   (IPSC). (G) Population data of evoked IPSC amplitudes from +/+ (black) and *an/an* (grey)

924   autaptic cortical neurons. (H) Responses from +/+ (black) and *an/an* (grey) cortical neurons

925   during 5 s application of 500 mM sucrose. (I) Box plot of readily releasable pool (RRP) and (J)

926   average vesicular release probability (P_{vr} = IPSC charge / RRP charge) in autaptic +/+ and

927   *an/an* neurons. (K) Traces of mIPSCs from +/+ (black) and *an/an* (grey) neurons. (L and M)

928   Box plots of mIPSC frequencies (L) and mEPSC amplitudes (M). Data was collected from 2

929   independent cultures.

930
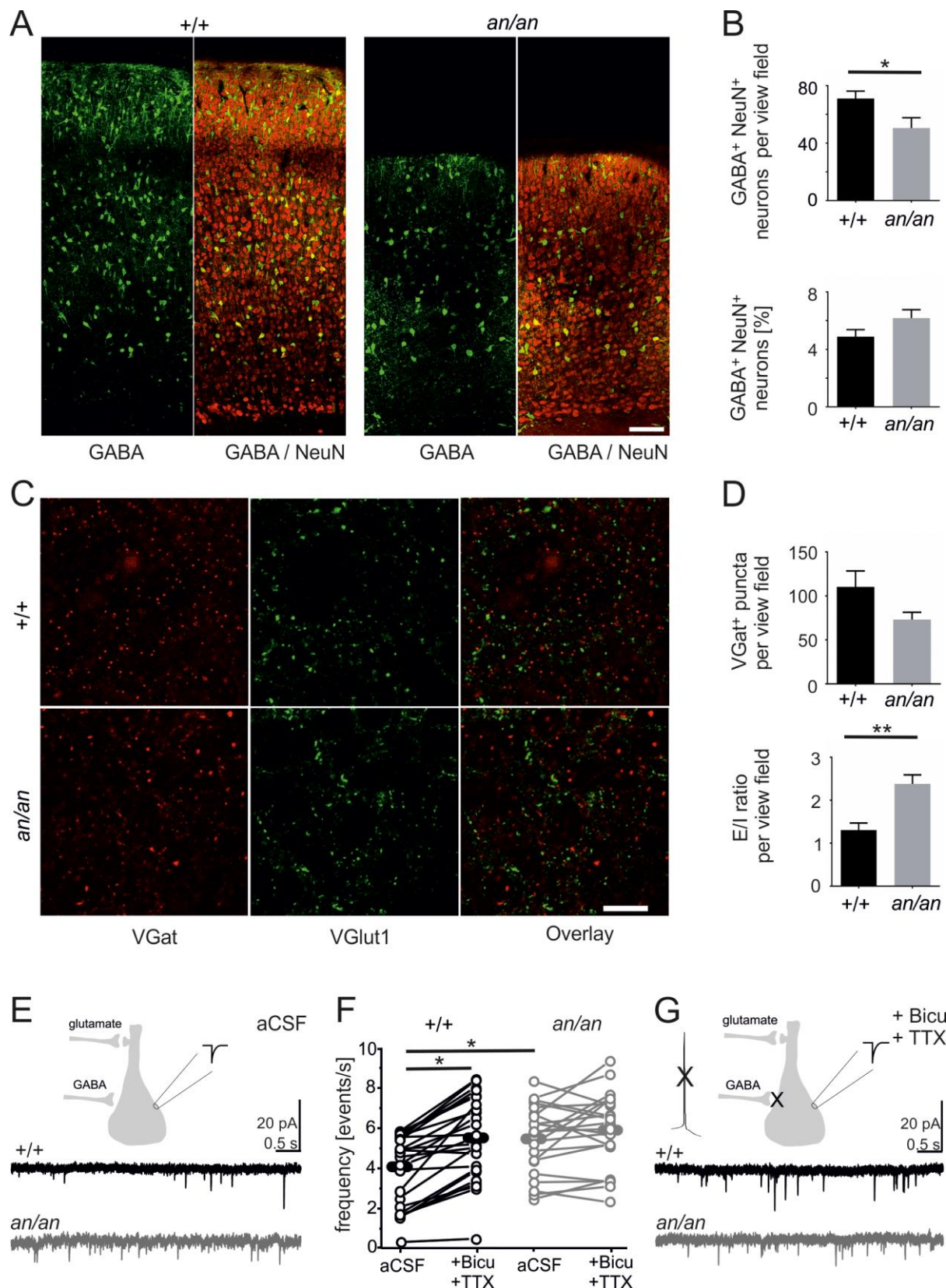
Fig 7. Loss of GABAergic input adjusts excitatory drive in neocortical layer 2/3 pyramidal

neurons of +/+ and *an/an* animals. (A) Coronal brain sections of P6-7 littermate animals stained

for the interneuron/astrocyte marker GABA (green) and the neuronal marker NeuN (red)

934   (immunofluorescence images, scale bar 100 µm). (B) The total number GABA$^+$ cells per view-

935   field is reduced in *an/an* mice but the proportion of these cells in relation to total NeuN$^+$ neurons

936   per view-field is comparable to +/+ mice. Note that there is no overlap of GABA and GFAP (Fig

937   S4), rendering an astrocytic contribution to GABA$^+$ cells unlikely. (C) Images of layer 2/3 areas

938   (0.002 mm^2) of parietal cortices from littermate animals stained for VGlut1 (excitatory-

939   presynaptic) and VGat (inhibitory-presynaptic) markers (confocal images, scale bar 10 µm).

940   (D) The trend towards reduced number of inhibitory synapses contributes to an increased E/I

941   ratio at layer 2/3 areas in *an/an* mice n = 15 images from 6 +/+ animals and 20 images from 6

942   *an/an* animals). (E and G) Comparative example of mEPSCs recorded at -60 mV before (E)

943   and after blocking spontaneous action potentials and GABA$_A$ receptors with tetrodotoxin and

944   bicuculline (+Bicu +TTX) (G) in +/+ (*black*) and *an/an* (*grey*) neurons. (F) Line series plots of

945   PSC frequencies before (*aCSF*) and after blocking spontaneous action potentials and

946   GABAergic transmission (*+Bicu +TTX*). In neurons from +/+ mice the EPSC frequency

947   increased, whereas EPSC frequency remained comparable in *an/an*. Note that this differential

948   effect led to similar total excitatory charge transfer (not shown) and mEPSCs frequency. The

949   average amplitude was similar in +/+ and *an/an* pyramidal neurons (n = 30 +/+ and 26 *an/an*

950   neurons from 4 animals/group). The serial resistance was comparable ($R_{s+/+}$ = 12.2 ± 0.8 MΩ

951   *vs.* $R_{s an/an}$ = 11.5 ± 0.8 MΩ, p = 0.8, MWU; not shown).

Supplementary figures and figure legends
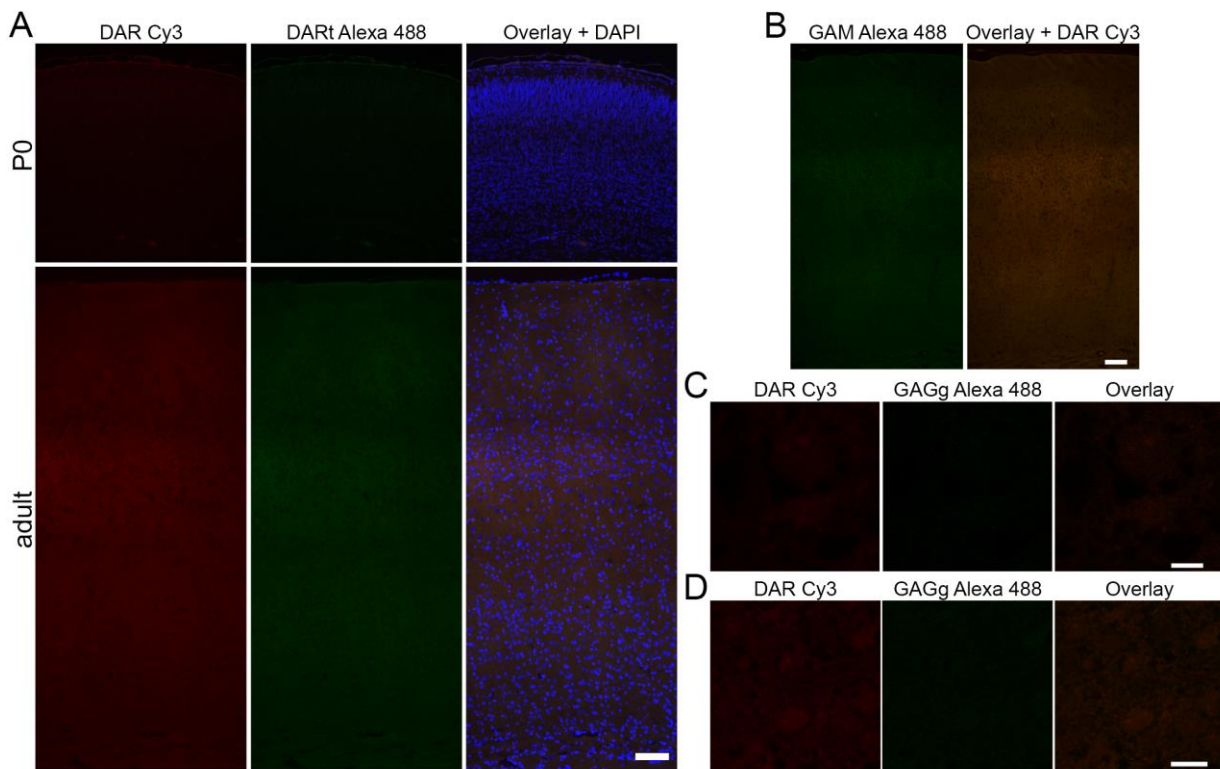
953

954 **Fig S1.** Negative control staining for Cux1, Ctip2, GABA, NeuN, PSD95, VGlut1 and VGat and

955 antibodies used in this study. (A) Secondary antibody staining for donkey anti-rabbit IgG Cy3

956 and donkey anti-Rat IgG Alexa Fluor 488 used to detect Cux1 and Ctip2 in (Fig 2A) respectively

957 (immunofluorescence images, scale bar 100 μm). (B) Secondary antibody staining for goat

958 anti-mouse IgG1 Alexa Fluor 488 and donkey anti-rabbit IgG Cy3 used to detect GABA and

959 NeuN in (Fig 7A) respectively (immunofluorescence images, scale bar 100 μm). (C) Secondary

960 antibody staining for donkey anti-rabbit IgG Cy3 and goat anti-guinea pig IgG Alexa Fluor 488

961 used to detect PSD95 and VGlut1 in (Fig 4K) respectively (confocal images, scale bar 2 μm).

962 Secondary antibody staining for donkey anti-rabbit IgG Cy3 and goat anti-guinea pig IgG Alexa

963 Fluor 488 used to detect VGat and VGlut1 in (Fig 7C) respectively (confocal images, scale bar
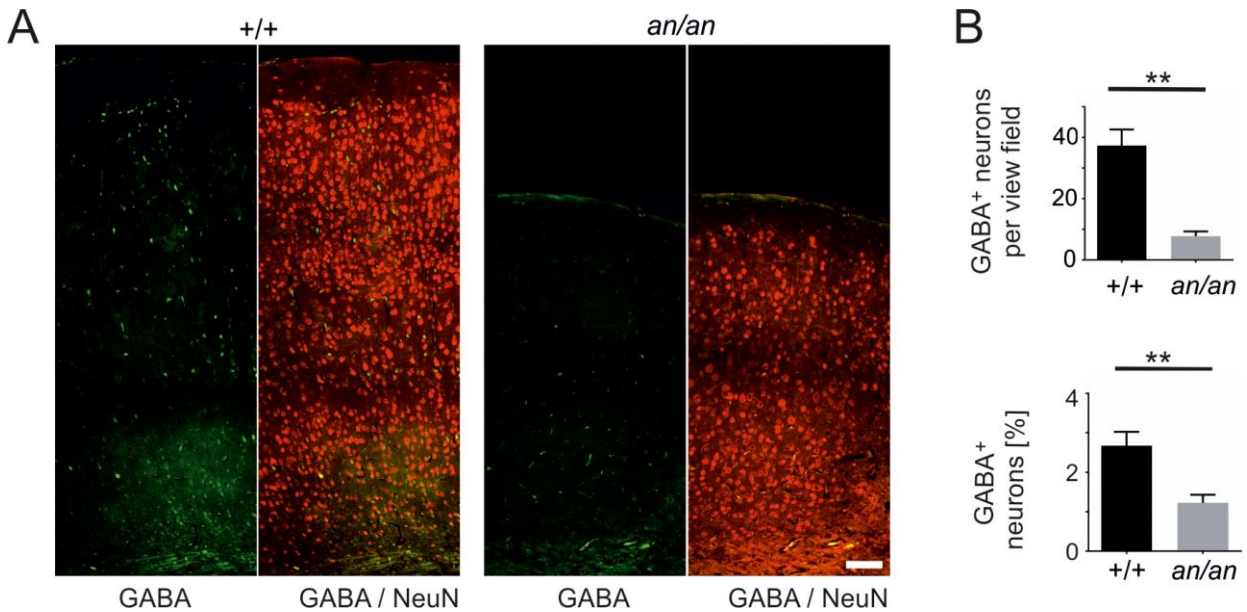
964 10 μm).

965
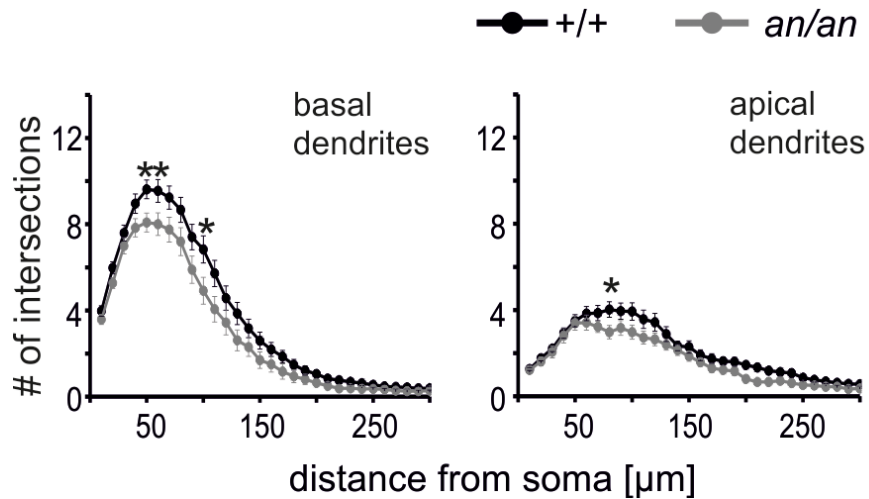
Fig S2. Reduced dendritic complexity of layer 2/3 pyramidal neurons from *an/an* mature

neocortex. Sholl analysis shows that less dendritic intersections 50 - 110 µm from the soma in

an/an mice (Fig 3B) is due to a reduction in apical and basal dendrites (n = 44 +/+ and 39 *an/an*

neurons from 6 +/+ and 4 *an/an* animals).

970

971

Fig S3. Loss of GABAergic input adjusts excitatory drive in neocortical layer 2/3 pyramidal

neurons of +/+ and *an/an* animals. (A) Coronal brain sections of adult littermate animals stained

for the interneuron marker GABA (GABA+ green) and the neuronal marker NeuN (red)

(immunofluorescence images, scale bar 100 µm). (B) The total number of interneurons positive

for GABA per view-field and the proportion of these cells in relation to total NeuN+ neurons per

view-field is reduced in *an/an* mice.

GABA	GABA / GFAP	GABA	GABA / GFAP

978
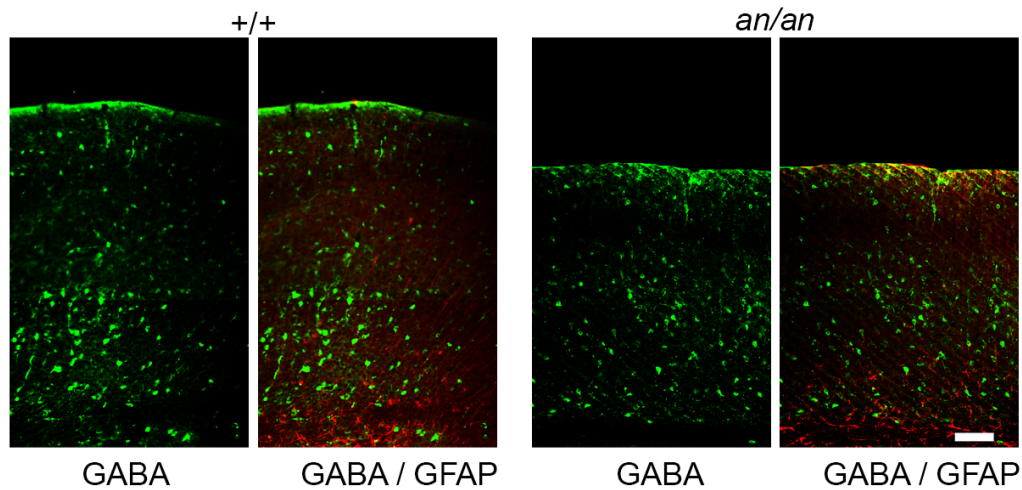
Fig S4. No gross difference in the astrocyte distribution between +/+ and *an/an* animals. Coronal brain sections of P6-7 littermate animals stained for the interneuron marker GABA (GABA+ green) and the radial glial / astrocyte marker GFAP (GFAP+ red) (immunofluorescence images, scale bar 100 μm). At this developmental age, only very few GFAP+ astrocytes were detected in the cortex and there was no GFAP/GABA overlap.

984 **Supplementary tables**

985 **Table S1.** Data means and two-way ANOVAs for Fig 1 and Fig 2.

Figure and graph	Analyzed data / marker	P0 (Mean ± SEM)		Adult (Mean ± SEM)		Two-way ANOVA		
		+/+	*an/an*	+/+	*an/an*	Interaction	Genotype	Age
Fig 1B. left	Neocortical area	3.9 ± 0.1 mm^2	1.8 ± 0.2 mm^2	29.4 ± 1.0 mm^2	14.7 ± 1.0 mm^2	P < 0.0001	P < 0.0001	P < 0.0001
Fig 1B. right	Cortical thickness	579.1 ± 13.2 µm	388.3 ± 17.8 µm	1381 ± 48.2 µm	934.2 ± 53.4 µm	P = 0.0027	P < 0.0001	P < 0.0001
Fig 2B	DAPI$^+$	2321 ± 102.1 cells	1823 ± 77.1 cells	1929 ± 73.1 cells	959.6 ± 29.5 cells	P = 0.0045	P < 0.0001	P < 0.0001
Fig 2C. left	Cux1$^+$	132.3 ± 5.2 µm	87.1 ± 6.7 µm	533.2 ± 40.9 µm	298.4 ± 15.6 µm	P = 0.0003	P < 0.0001	P < 0.0001
	Ctip2$^+$	333.3 ± 12.3 µm	261.9 ± 11.5 µm	621.4 ± 29.5 µm	462.0 ± 28.4 µm	P = 0.0585	P < 0.0001	P < 0.0001
Fig 2C. right	Cux1$^+$	25.7 ± 1 %	21.5 ± 1.2%	36.4 ± 1.2 %	30.9 ± 1%	P = 0.5614	P = 0.0002	P < 0.0001
	Ctip2$^+$	64.6 ± 1.4 %	64.8 ± 1.2 %	43 ± 1.7 %	47.5 ± 0.8 %	P = 0.1183	P = 0.0855	P < 0.0001
Fig 2D. left	Cux1$^+$	477.3 ± 51.2 neurons	304.4 ± 26.4 neurons	462.3 ± 33.3 neurons	213.3 ± 22 neurons	P = 0.2883	P < 0.0001	P = 0.1431
	Ctip2$^+$	675.0 ± 27.8 neurons	516 ± 33.9 neurons	263.3 ± 28.1 neurons	151 ± 10.1 neurons	P = 0.3873	P < 0.0001	P < 0.0001
Fig 2D. right	Cux1$^+$	20.3 ± 1.5 %	16.6 ± 1.1%	24.2 ± 2.1 %	22.2 ± 2.1%	P = 0.6456	P = 0.1169	P = 0.0130
	Ctip2$^+$	29.2 ± 1.1 %	28.2 ± 1.2%	13.6 ± 1.2 %	15.9 ± 1.3%	P = 0.1737	P = 0.5814	P < 0.0001

986

987 **Table S2.** Age correlation analysis.

Analyzed data	Prob>F	Pearson's r
frequency	0.83	-0.04
amplitude	0.73	0.07
decay time	0.75	-0.06
Cap	0.06	0.36
Rinput	0.46	-0.15
rheobase	0.82	-0.05
slope	0.34	0.21
membr	0.24	-0.28
GABA #	0.60	-0.19
GABA %	0.40	-0.30
neocortical area	0.93	0.02
cortical thickness	0.88	-0.04
Cux1 #	0.53	-0.18
Ctip2 #	0.54	0.18
DAPI #	0.75	-0.09
Cux1 %	0.70	-0.11
Ctip2 %	0.16	0.39
Cux1 thickness	0.87	-0.05
Ctip2 thickness	0.52	0.19
DAPI thickness	0.93	0.03
Cux1 thickness %	0.50	-0.19
Ctip2 thickness %	0.36	0.27
primary dendrites	0.60	0.20
secondary dendrites	0.37	-0.34
tertiary dendrites	0.59	0.21
spine density	0.14	-0.53
Mushroom spines %	0.07	-0.63
Stubby spines %	0.33	0.36
Thin spines %	0.92	-0.04

988